

AD-A110 495 VIRGINIA POLYTECHNIC INST AND STATE UNIV BLACKSBURG --ETC F/G 20/4
ON THE AERODYNAMICS OF WINDBLAST.(U)
NOV 81 D J SCHNECK AFOSR-78-3706

UNCLASSIFIED VPI-E-81-31

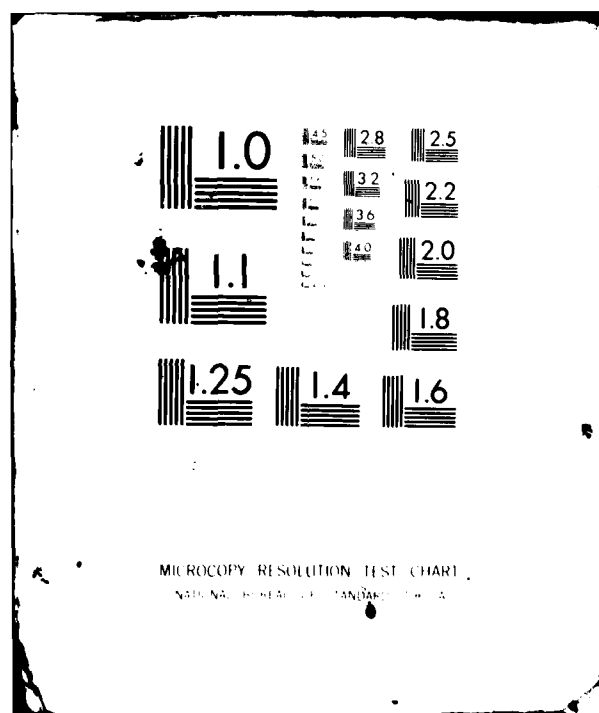
AFOSR-TR-82-0031

NL

1.1
AS
20/4



END
DATE
FILMED
3 82
DTIC



AD A110495



AFOSR
AFOSR GRANT NUMBER 78-3706
FINAL TECHNICAL REPORT
NOVEMBER 13, 1981

DTIC
FEB 1 1982
H

VPI-E-81-31

ON THE AERODYNAMICS
OF WINDBLAST

Daniel J. Schneck, Ph.D.
Professor of Engineering Science and Mechanics
Head, Biomedical Engineering Program
Virginia Polytechnic Institute and State University
Department of Engineering Science and Mechanics
227 Norris Hall
Blacksburg, Virginia 24061

AIR FORCE OFFICE OF SCIENTIFIC RESEARCH (AFSC)
NOTICE OF TRANSMITTAL TO DTIC
This technical report has been reviewed and is
approved for public release IAW AFR 190-12.
Distribution is unlimited.
MATTHEW J. KERPER
Chief, Technical Information Division

AFOSR (AFSC) USAF-NL
Bolling Air Force Base
D.C. 20332

4.4.122

SECTION I

INTRODUCTION

In two previous reports (Schneck, 1976, 1979) a mathematical theory was developed in order to calculate the aerodynamic loading to which a pilot is exposed during high speed ejections. Neglecting the effects of flow separation, preliminary results suggested that the pilot's musculo-skeletal resistance is not likely to withstand the tendency for dislodgement from a restraining surface if he is ejecting at Mach numbers exceeding 0.72. More specifically, the aerodynamic dislodging (windblast) force, F (in lbs.), that is generated at an altitude of 10,000 feet can be described by the equation:

$$F = 1148M^2 \sin^2 \alpha, \quad (1)$$

where α is the angle at which a pilot's limb intercepts an air stream moving at Mach M .

Recently (Schneck, 1979) the mathematical theory of windblast was modified to include some effects of flow separation. In the report that follows, these effects are examined in greater detail, particularly as they affect the time-course of limb dislodging forces after the onset of windblast.

SECTION II

VORTEX PATTERNS FOLLOWING DISLODGEEMENT

Consider the situation depicted in Figure 1. This illustrates the instantaneous streamline pattern that characterizes the cross-flow over two circular-cylindrical body segments in line contact with one another at time $t = 0$. That is, at the moment this limb-to-limb or limb-to-restraining surface configuration intercepts a high-speed cross-flow, the streamline pattern is initially inviscid, a boundary layer has had no time to grow and the flow starts out essentially attached. However, this situation will last momentarily, since stagnation of the flow along the line contact between the two cylinders will result in the generation of relatively large forces which tend to pull the cylinders apart. In fact, equation (1) predicts that, for $\alpha = 90^\circ$, beyond Mach 0.72 the forces so generated will exceed the amount by which an average pilot can resist the tendency to have his limbs pulled

apart. Thus, it is likely that for $t = 0^+$, a fraction of a second after the flow is intercepted, the situation depicted in Figure 2A prevails. Here, the cylinders are shown separated by a very small distance, b , simulating the beginning of flail resulting from windblast.

The configuration illustrated in Figure 2A produces a venturi effect. The fluid passing through the throat between the cylinders separated a slight distance b is accelerated and exits the gap with some velocity, u_2 . On the

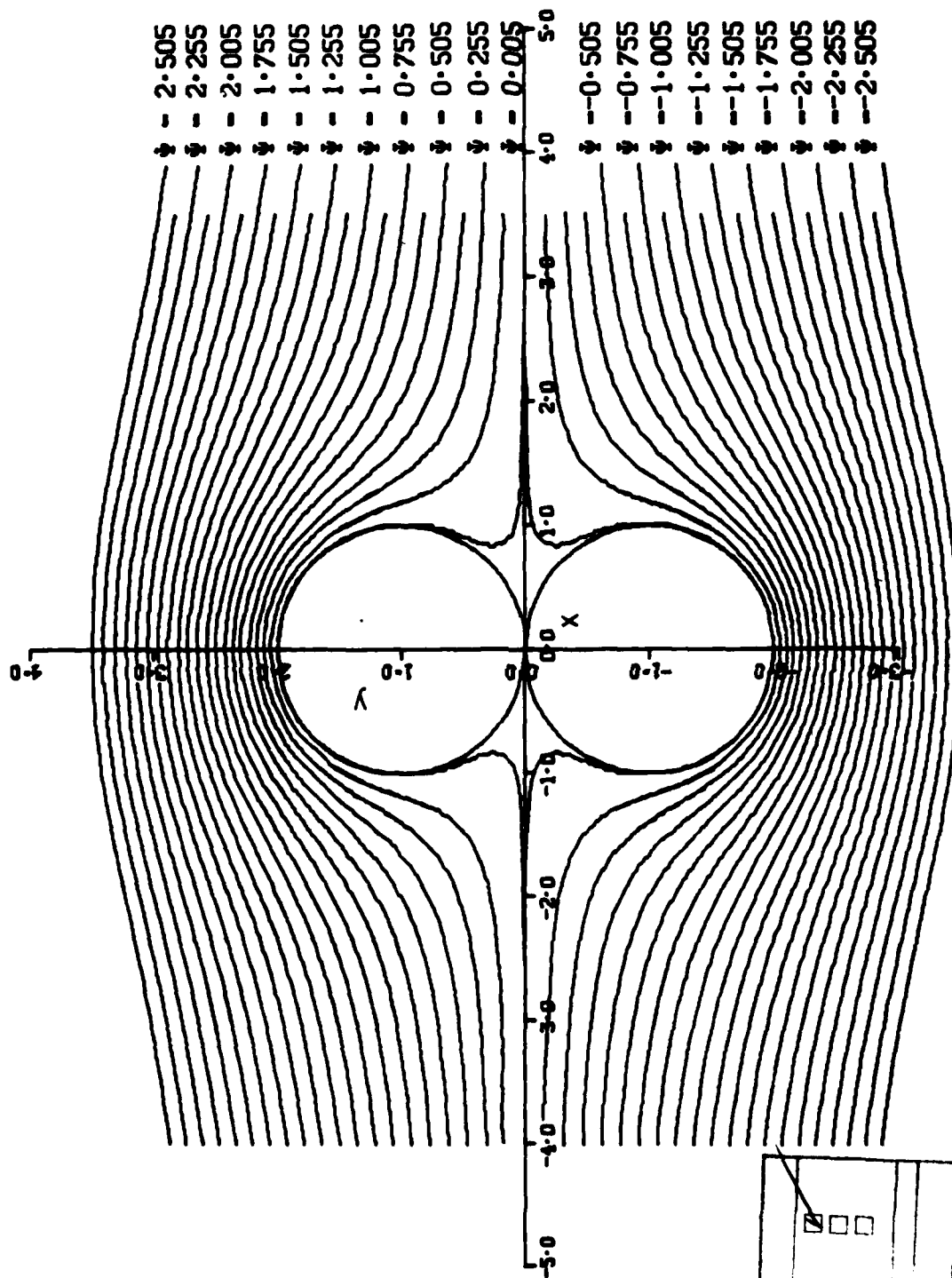


Figure 1: Instantaneous Streamline Pattern that Characterizes the Cross-Flow over two Circular-Cylindrical Body Segments in Line Contact with One Another at Time $t = 0$ (the Onset of Limb/Flow Interaction).

Accession For	
THIS COPY	<input checked="" type="checkbox"/>
FIG 1	<input type="checkbox"/>
FIG 2	<input type="checkbox"/>
FIG 3	<input type="checkbox"/>
FIG 4	<input type="checkbox"/>
FIG 5	<input type="checkbox"/>
FIG 6	<input type="checkbox"/>
FIG 7	<input type="checkbox"/>
FIG 8	<input type="checkbox"/>
FIG 9	<input type="checkbox"/>
FIG 10	<input type="checkbox"/>
FIG 11	<input type="checkbox"/>
FIG 12	<input type="checkbox"/>
FIG 13	<input type="checkbox"/>
FIG 14	<input type="checkbox"/>
FIG 15	<input type="checkbox"/>
FIG 16	<input type="checkbox"/>
FIG 17	<input type="checkbox"/>
FIG 18	<input type="checkbox"/>
FIG 19	<input type="checkbox"/>
FIG 20	<input type="checkbox"/>
FIG 21	<input type="checkbox"/>
FIG 22	<input type="checkbox"/>
FIG 23	<input type="checkbox"/>
FIG 24	<input type="checkbox"/>
FIG 25	<input type="checkbox"/>
FIG 26	<input type="checkbox"/>
FIG 27	<input type="checkbox"/>
FIG 28	<input type="checkbox"/>
FIG 29	<input type="checkbox"/>
FIG 30	<input type="checkbox"/>
FIG 31	<input type="checkbox"/>
FIG 32	<input type="checkbox"/>
FIG 33	<input type="checkbox"/>
FIG 34	<input type="checkbox"/>
FIG 35	<input type="checkbox"/>
FIG 36	<input type="checkbox"/>
FIG 37	<input type="checkbox"/>
FIG 38	<input type="checkbox"/>
FIG 39	<input type="checkbox"/>
FIG 40	<input type="checkbox"/>
FIG 41	<input type="checkbox"/>
FIG 42	<input type="checkbox"/>
FIG 43	<input type="checkbox"/>
FIG 44	<input type="checkbox"/>
FIG 45	<input type="checkbox"/>
FIG 46	<input type="checkbox"/>
FIG 47	<input type="checkbox"/>
FIG 48	<input type="checkbox"/>
FIG 49	<input type="checkbox"/>
FIG 50	<input type="checkbox"/>
FIG 51	<input type="checkbox"/>
FIG 52	<input type="checkbox"/>
FIG 53	<input type="checkbox"/>
FIG 54	<input type="checkbox"/>
FIG 55	<input type="checkbox"/>
FIG 56	<input type="checkbox"/>
FIG 57	<input type="checkbox"/>
FIG 58	<input type="checkbox"/>
FIG 59	<input type="checkbox"/>
FIG 60	<input type="checkbox"/>
FIG 61	<input type="checkbox"/>
FIG 62	<input type="checkbox"/>
FIG 63	<input type="checkbox"/>
FIG 64	<input type="checkbox"/>
FIG 65	<input type="checkbox"/>
FIG 66	<input type="checkbox"/>
FIG 67	<input type="checkbox"/>
FIG 68	<input type="checkbox"/>
FIG 69	<input type="checkbox"/>
FIG 70	<input type="checkbox"/>
FIG 71	<input type="checkbox"/>
FIG 72	<input type="checkbox"/>
FIG 73	<input type="checkbox"/>
FIG 74	<input type="checkbox"/>
FIG 75	<input type="checkbox"/>
FIG 76	<input type="checkbox"/>
FIG 77	<input type="checkbox"/>
FIG 78	<input type="checkbox"/>
FIG 79	<input type="checkbox"/>
FIG 80	<input type="checkbox"/>
FIG 81	<input type="checkbox"/>
FIG 82	<input type="checkbox"/>
FIG 83	<input type="checkbox"/>
FIG 84	<input type="checkbox"/>
FIG 85	<input type="checkbox"/>
FIG 86	<input type="checkbox"/>
FIG 87	<input type="checkbox"/>
FIG 88	<input type="checkbox"/>
FIG 89	<input type="checkbox"/>
FIG 90	<input type="checkbox"/>
FIG 91	<input type="checkbox"/>
FIG 92	<input type="checkbox"/>
FIG 93	<input type="checkbox"/>
FIG 94	<input type="checkbox"/>
FIG 95	<input type="checkbox"/>
FIG 96	<input type="checkbox"/>
FIG 97	<input type="checkbox"/>
FIG 98	<input type="checkbox"/>
FIG 99	<input type="checkbox"/>
FIG 100	<input type="checkbox"/>
FIG 101	<input type="checkbox"/>
FIG 102	<input type="checkbox"/>
FIG 103	<input type="checkbox"/>
FIG 104	<input type="checkbox"/>
FIG 105	<input type="checkbox"/>
FIG 106	<input type="checkbox"/>
FIG 107	<input type="checkbox"/>
FIG 108	<input type="checkbox"/>
FIG 109	<input type="checkbox"/>
FIG 110	<input type="checkbox"/>
FIG 111	<input type="checkbox"/>
FIG 112	<input type="checkbox"/>
FIG 113	<input type="checkbox"/>
FIG 114	<input type="checkbox"/>
FIG 115	<input type="checkbox"/>
FIG 116	<input type="checkbox"/>
FIG 117	<input type="checkbox"/>
FIG 118	<input type="checkbox"/>
FIG 119	<input type="checkbox"/>
FIG 120	<input type="checkbox"/>
FIG 121	<input type="checkbox"/>
FIG 122	<input type="checkbox"/>
FIG 123	<input type="checkbox"/>
FIG 124	<input type="checkbox"/>
FIG 125	<input type="checkbox"/>
FIG 126	<input type="checkbox"/>
FIG 127	<input type="checkbox"/>
FIG 128	<input type="checkbox"/>
FIG 129	<input type="checkbox"/>
FIG 130	<input type="checkbox"/>
FIG 131	<input type="checkbox"/>
FIG 132	<input type="checkbox"/>
FIG 133	<input type="checkbox"/>
FIG 134	<input type="checkbox"/>
FIG 135	<input type="checkbox"/>
FIG 136	<input type="checkbox"/>
FIG 137	<input type="checkbox"/>
FIG 138	<input type="checkbox"/>
FIG 139	<input type="checkbox"/>
FIG 140	<input type="checkbox"/>
FIG 141	<input type="checkbox"/>
FIG 142	<input type="checkbox"/>
FIG 143	<input type="checkbox"/>
FIG 144	<input type="checkbox"/>
FIG 145	<input type="checkbox"/>
FIG 146	<input type="checkbox"/>
FIG 147	<input type="checkbox"/>
FIG 148	<input type="checkbox"/>
FIG 149	<input type="checkbox"/>
FIG 150	<input type="checkbox"/>
FIG 151	<input type="checkbox"/>
FIG 152	<input type="checkbox"/>
FIG 153	<input type="checkbox"/>
FIG 154	<input type="checkbox"/>
FIG 155	<input type="checkbox"/>
FIG 156	<input type="checkbox"/>
FIG 157	<input type="checkbox"/>
FIG 158	<input type="checkbox"/>
FIG 159	<input type="checkbox"/>
FIG 160	<input type="checkbox"/>
FIG 161	<input type="checkbox"/>
FIG 162	<input type="checkbox"/>
FIG 163	<input type="checkbox"/>
FIG 164	<input type="checkbox"/>
FIG 165	<input type="checkbox"/>
FIG 166	<input type="checkbox"/>
FIG 167	<input type="checkbox"/>
FIG 168	<input type="checkbox"/>
FIG 169	<input type="checkbox"/>
FIG 170	<input type="checkbox"/>
FIG 171	<input type="checkbox"/>
FIG 172	<input type="checkbox"/>
FIG 173	<input type="checkbox"/>
FIG 174	<input type="checkbox"/>
FIG 175	<input type="checkbox"/>
FIG 176	<input type="checkbox"/>
FIG 177	<input type="checkbox"/>
FIG 178	<input type="checkbox"/>
FIG 179	<input type="checkbox"/>
FIG 180	<input type="checkbox"/>
FIG 181	<input type="checkbox"/>
FIG 182	<input type="checkbox"/>
FIG 183	<input type="checkbox"/>
FIG 184	<input type="checkbox"/>
FIG 185	<input type="checkbox"/>
FIG 186	<input type="checkbox"/>
FIG 187	<input type="checkbox"/>
FIG 188	<input type="checkbox"/>
FIG 189	<input type="checkbox"/>
FIG 190	<input type="checkbox"/>
FIG 191	<input type="checkbox"/>
FIG 192	<input type="checkbox"/>
FIG 193	<input type="checkbox"/>
FIG 194	<input type="checkbox"/>
FIG 195	<input type="checkbox"/>
FIG 196	<input type="checkbox"/>
FIG 197	<input type="checkbox"/>
FIG 198	<input type="checkbox"/>
FIG 199	<input type="checkbox"/>
FIG 200	<input type="checkbox"/>
FIG 201	<input type="checkbox"/>
FIG 202	<input type="checkbox"/>
FIG 203	<input type="checkbox"/>
FIG 204	<input type="checkbox"/>
FIG 205	<input type="checkbox"/>
FIG 206	<input type="checkbox"/>
FIG 207	<input type="checkbox"/>
FIG 208	<input type="checkbox"/>
FIG 209	<input type="checkbox"/>
FIG 210	<input type="checkbox"/>
FIG 211	<input type="checkbox"/>
FIG 212	<input type="checkbox"/>
FIG 213	<input type="checkbox"/>
FIG 214	<input type="checkbox"/>
FIG 215	<input type="checkbox"/>
FIG 216	<input type="checkbox"/>
FIG 217	<input type="checkbox"/>
FIG 218	<input type="checkbox"/>
FIG 219	<input type="checkbox"/>
FIG 220	<input type="checkbox"/>
FIG 221	<input type="checkbox"/>
FIG 222	<input type="checkbox"/>
FIG 223	<input type="checkbox"/>
FIG 224	<input type="checkbox"/>
FIG 225	<input type="checkbox"/>
FIG 226	<input type="checkbox"/>
FIG 227	<input type="checkbox"/>
FIG 228	<input type="checkbox"/>
FIG 229	<input type="checkbox"/>
FIG 230	<input type="checkbox"/>
FIG 231	<input type="checkbox"/>
FIG 232	<input type="checkbox"/>
FIG 233	<input type="checkbox"/>
FIG 234	<input type="checkbox"/>
FIG 235	<input type="checkbox"/>
FIG 236	<input type="checkbox"/>
FIG 237	<input type="checkbox"/>
FIG 238	<input type="checkbox"/>
FIG 239	<input type="checkbox"/>
FIG 240	<input type="checkbox"/>
FIG 241	<input type="checkbox"/>
FIG 242	<input type="checkbox"/>
FIG 243	<input type="checkbox"/>
FIG 244	<input type="checkbox"/>
FIG 245	<input type="checkbox"/>
FIG 246	<input type="checkbox"/>
FIG 247	<input type="checkbox"/>
FIG 248	<input type="checkbox"/>
FIG 249	<input type="checkbox"/>
FIG 250	<input type="checkbox"/>
FIG 251	<input type="checkbox"/>
FIG 252	<input type="checkbox"/>
FIG 253	<input type="checkbox"/>
FIG 254	<input type="checkbox"/>
FIG 255	<input type="checkbox"/>
FIG 256	<input type="checkbox"/>
FIG 257	<input type="checkbox"/>
FIG 258	<input type="checkbox"/>
FIG 259	<input type="checkbox"/>
FIG 260	<input type="checkbox"/>
FIG 261	<input type="checkbox"/>
FIG 262	<input type="checkbox"/>
FIG 263	<input type="checkbox"/>
FIG 264	<input type="checkbox"/>
FIG 265	<input type="checkbox"/>
FIG 266	<input type="checkbox"/>
FIG 267	<input type="checkbox"/>
FIG 268	<input type="checkbox"/>
FIG 269	<input type="checkbox"/>
FIG 270	<input type="checkbox"/>
FIG 271	<input type="checkbox"/>
FIG 272	<input type="checkbox"/>
FIG 273	<input type="checkbox"/>
FIG 274	<input type="checkbox"/>
FIG 275	<input type="checkbox"/>
FIG 276	<input type="checkbox"/>
FIG 277	<input type="checkbox"/>
FIG 278	<input type="checkbox"/>
FIG 279	<input type="checkbox"/>
FIG 280	<input type="checkbox"/>
FIG 281	<input type="checkbox"/>
FIG 282	<input type="checkbox"/>
FIG 283	<input type="checkbox"/>
FIG 284	<input type="checkbox"/>
FIG 285	<input type="checkbox"/>
FIG 286	<input type="checkbox"/>
FIG 287	<input type="checkbox"/>
FIG 288	<input type="checkbox"/>
FIG 289	<input type="checkbox"/>
FIG 290	<input type="checkbox"/>
FIG 291	<input type="checkbox"/>
FIG 292	<input type="checkbox"/>
FIG 293	<input type="checkbox"/>
FIG 294	<input type="checkbox"/>
FIG 295	<input type="checkbox"/>
FIG 296	<input type="checkbox"/>
FIG 297	<input type="checkbox"/>
FIG 298	<input type="checkbox"/>
FIG 299	<input type="checkbox"/>
FIG 300	<input type="checkbox"/>
FIG 301	<input type="checkbox"/>
FIG 302	<input type="checkbox"/>
FIG 303	<input type="checkbox"/>
FIG 304	<input type="checkbox"/>
FIG 305	<input type="checkbox"/>
FIG 306	<input type="checkbox"/>
FIG 307	<input type="checkbox"/>
FIG 308	<input type="checkbox"/>
FIG 309	<input type="checkbox"/>
FIG 310	<input type="checkbox"/>
FIG 311	<input type="checkbox"/>
FIG 312	<input type="checkbox"/>
FIG 313	<input type="checkbox"/>
FIG 314	<input type="checkbox"/>
FIG 315	<input type="checkbox"/>
FIG 316	<input type="checkbox"/>
FIG 317	<input type="checkbox"/>
FIG 318	<input type="checkbox"/>
FIG 319	<input type="checkbox"/>
FIG 320	<input type="checkbox"/>
FIG 321	<input type="checkbox"/>
FIG 322	<input type="checkbox"/>
FIG 323	<input type="checkbox"/>
FIG 324	<input type="checkbox"/>
FIG 325	<input type="checkbox"/>
FIG 326	<input type="checkbox"/>
FIG 327	<input type="checkbox"/>
FIG 328	<input type="checkbox"/>
FIG 329	<input type="checkbox"/>
FIG 330	<input type="checkbox"/>
FIG 331	<input type="checkbox"/>
FIG 332	<input type="checkbox"/>
FIG 333	<input type="checkbox"/>
FIG 334	<input type="checkbox"/>
FIG 335	<input type="checkbox"/>
FIG 336	<input type="checkbox"/>
FIG 337	<input type="checkbox"/>
FIG 338	<input type="checkbox"/>
FIG 339	<input type="checkbox"/>
FIG 340	<input type="checkbox"/>
FIG 341	<input type="checkbox"/>
FIG 342	<input type="checkbox"/>
FIG 343	<input type="checkbox"/>
FIG 344	<input type="checkbox"/>
FIG 345	<input type="checkbox"/>
FIG 346	<input type="checkbox"/>
FIG 347	<input type="checkbox"/>
FIG 348	<input type="checkbox"/>
FIG 349	<input type="checkbox"/>
FIG 350	<input type="checkbox"/>
FIG 351	<input type="checkbox"/>
FIG 352	<input type="checkbox"/>
FIG 353	<input type="checkbox"/>
FIG 354	<input type="checkbox"/>
FIG 355	<input type="checkbox"/>
FIG 356	<input type="checkbox"/>
FIG 357	<input type="checkbox"/>
FIG 358	<input type="checkbox"/>
FIG 359	<input type="checkbox"/>
FIG 360	<input type="checkbox"/>
FIG 361	<input type="checkbox"/>
FIG 362	<input type="checkbox"/>
FIG 363	<input type="checkbox"/>
FIG 364	<input type="checkbox"/>
FIG 365	<input type="checkbox"/>
FIG 366	<input type="checkbox"/>
FIG 367	<input type="checkbox"/>
FIG 368	<input type="checkbox"/>
FIG 369	<input type="checkbox"/>
FIG 370	<input type="checkbox"/>
FIG 371	<input type="checkbox"/>
FIG 372	<input type="checkbox"/>
FIG 373	<input type="checkbox"/>
FIG 374	<input type="checkbox"/>
FIG 375	<input type="checkbox"/>
FIG 376	<input type="checkbox"/>
FIG 377	<input type="checkbox"/>
FIG 378	<input type="checkbox"/>
FIG 379	<input type="checkbox"/>
FIG 380	<input type="checkbox"/>
FIG 381	<input type="checkbox"/>
FIG 382	<input type="checkbox"/>
FIG 383	<input type="checkbox"/>
FIG 384	<input type="checkbox"/>
FIG 385	<input type="checkbox"/>
FIG 386	<input type="checkbox"/>
FIG 387	<input type="checkbox"/>
FIG 388	<input type="checkbox"/>
FIG 389	<input type="checkbox"/>
FIG 390	<input type="checkbox"/>
FIG 391	<input type="checkbox"/>
FIG 392	<input type="checkbox"/>
FIG 393	<input type="checkbox"/>
FIG 394	<input type="checkbox"/>
FIG 395	<input type="checkbox"/>
FIG 396	<input type="checkbox"/>
FIG 397	<input type="checkbox"/>
FIG 398	<input type="checkbox"/>
FIG 399	<input type="checkbox"/>
FIG 400	<input type="checkbox"/>
FIG 401	<input type="checkbox"/>
FIG 402	<input type="checkbox"/>
FIG 403	<input type="checkbox"/>
FIG 404	<input type="checkbox"/>
FIG 405	<input type="checkbox"/>
FIG 406	<input type="checkbox"/>
FIG 407	<input type="checkbox"/>
FIG 408	<input type="checkbox"/>
FIG 409	<input type="checkbox"/>
FIG 410	<input type="checkbox"/>
FIG 411	<input type="checkbox"/>
FIG 412	<input type="checkbox"/>
FIG 413	<input type="checkbox"/>
FIG 414	<input type="checkbox"/>
FIG 415	<input type="checkbox"/>
FIG 416	<input type="checkbox"/>
FIG 417	<input type="checkbox"/>
FIG 418	<input type="checkbox"/>
FIG 419	<input type="checkbox"/>
FIG 420	<input type="checkbox"/>
FIG 421	<input type="checkbox"/>
FIG 422	<input type="checkbox"/>
FIG 423	<input type="checkbox"/>
FIG 424	<input type="checkbox"/>
FIG 425	<input type="checkbox"/>
FIG 426	<input type="checkbox"/>
FIG 427	<input type="checkbox"/>
FIG 428	<input type="checkbox"/>
FIG 429	<input type="checkbox"/>
FIG 430	<input type="checkbox"/>

other hand, the fluid diverted to the outside, not passing through the throat, circles around the cylinders and diffuses sharply on the downstream side, decelerating to some velocity $u_1 \ll u_2$. Thus, in the narrow region, y , where a streamline having velocity u_1 meets a streamline having velocity u_2 , there is a large velocity gradient which causes the fluid to roll up into a starting vortex, as shown in Figure 2B.

The starting vortex thus generated on each cylinder grows until it is eventually shed, leaving behind an equal and opposite circulation, Γ , about the cylinder as shown in Figure 2C. Note, however, that this circulation acts to retard fluid flow through the throat region while increasing the flow around the outer sides of the cylinders. It thus works against the venturi effect depicted in Figure 2A. The result is that, in time, the effect of the circulation is to make the fluid velocity on the outer sides of the cylinders greater than that between the cylinders. This reverses the velocity gradient illustrated in Figure 2A, such that vortices of opposite spin now roll up on the outer rim of the cylinders as the faster moving fluid encounters the slower moving streamlines diffusing out on the downstream side of the throat. This situation is illustrated in Figure 2D.

In turn, the second set of vortices generated as described above grows until it is shed, leaving behind an equal and opposite circulation which effectively cancels the circulation produced by the initial set of vortices. Thus, the picture essentially reverts back to that shown in Figure 2A and the whole process starts all over again. Over a period of time, then, when a steady-state has been reached, the wake behind the slightly separated double cylinder configuration can be described as containing a vortex street consisting of pairs of vortices shed periodically, 180° out of phase, and alternating in direction of rotation as illustrated in Figure 2E. The spacing between rows of vortices is designated as shown (h between rows 1 and 2 and 3 and 4, respectively and k between rows 2 and 3), while the distance between vortices in a row is given by ℓ .

The significance of the entire preceding discussion rests in the realization that the oscillatory nature of the flow described results in a corresponding oscillation of the forces tending to cause lateral motion of the two cylinders. That is, as vortices in rows 2 and 3 are shed, the circulation left behind causes u_2 to fall well below u_1 so the corresponding pressure p_2

$\gg p_1$ and there is a tendency for the cylinders to be driven apart from one

another. Conversely, as vortices in rows 1 and 4 are shed, the resulting circulation leads to $u_2 \gg u_1$, hence $p_2 \ll p_1$ and the cylinders are driven

towards one another. The net effect of the double vortex street in the wake is to produce a lateral vibration of the cylinders once they have separated due to flow stagnation forces. In the section that follows the theory for calculating the oscillating forces is developed following the method outlined by Landweber (1942) and Milne-Thomson (1955).

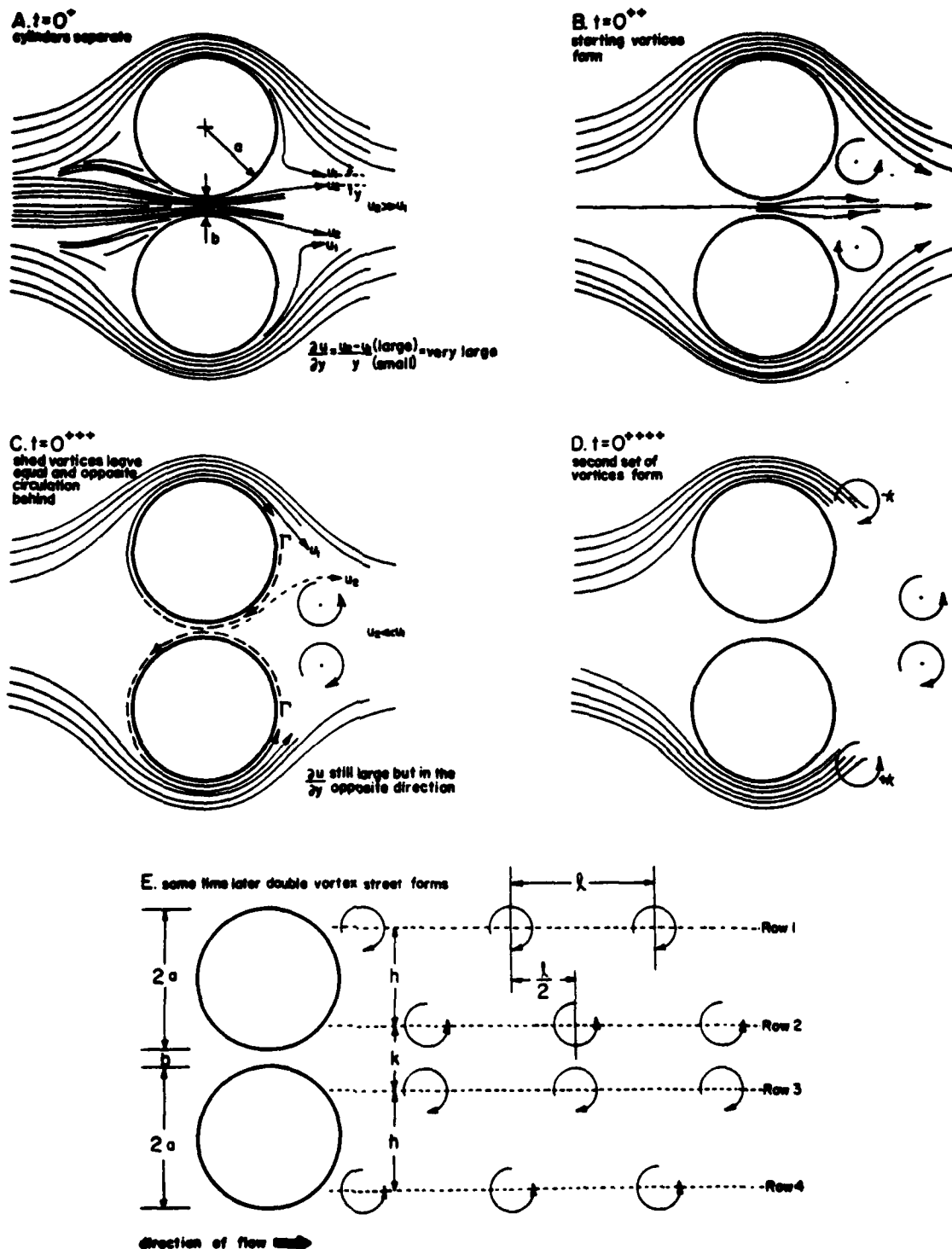


Figure 2: The Establishment of a Double Vortex Street Pattern Following the Interaction of the Configuration Depicted in Figure 1 with a High-Speed Cross-Flow.

SECTION III

DEVELOPMENT OF THEORY FOR CALCULATING OSCILLATING FORCES PRODUCING LATERAL DISPLACEMENT

Referring to Figure 3, consider a circular cylinder of radius "a" lying perpendicular to a uniform stream of velocity V and exposed to a circulation, Γ , of strength κ , such that $\Gamma = 2\pi\kappa$. The left-to-right streaming motion past the cylinder is given by the complex potential:

$$w_1 = -V[z + \frac{a^2}{z}] \quad , \quad z = x + iy = re^{i\theta} \quad (2)$$

while the clockwise circulation of strength κ about the cylinder is given by:

$$w_2 = -i\kappa \log \frac{z}{a}. \quad (3)$$

Combining these motions yields the complex potential:

$$w = w_1 + w_2 = -V[z + \frac{a^2}{z}] - i\kappa \log \frac{z}{a}. \quad (4)$$

Let there be a force $\vec{F} = F_x + iF_y$ acting per unit length on the cylinder as a result of the pressure distribution generated by the flow defined in equation (4). Then:

$$\vec{F} = \oint p d\vec{s} = \int p [idx + dy] = i \int (p) d[x - iy] = \int i p d\bar{z}. \quad (5)$$

Now, the steady-state form of Bernolli's equation is,

$$p + \frac{1}{2} \rho q^2 = \text{constant}, C_0 \quad (6)$$

where: $q^2 = \frac{dw}{dz} \frac{d\bar{w}}{d\bar{z}}$. But, since $w = \phi + i\psi$ and $\bar{w} = \phi - i\psi$, and since the

surface of the cylinder is the streamline $\psi = 0$, we note that on the surface $w = \bar{w}$, and so $dw = d\bar{w}$. Moreover, if interest is focused only in the pressure, p, that is due to the flow, q, i.e., we examine from the reference point p (or p minus some stagnation pressure p_0) = 0 when $q = 0$, then $C_0 = 0$, and equation (5) becomes:

$$\vec{F} = \int i(-\frac{1}{2} \rho q^2) d\bar{z} = \int i(-\frac{\rho}{2}) \frac{dw}{dz} \frac{d\bar{w}}{d\bar{z}} d\bar{z} = \oint -\frac{1}{2} \rho (\frac{dw}{dz})^2 dz \quad (7)$$

From equation (4):

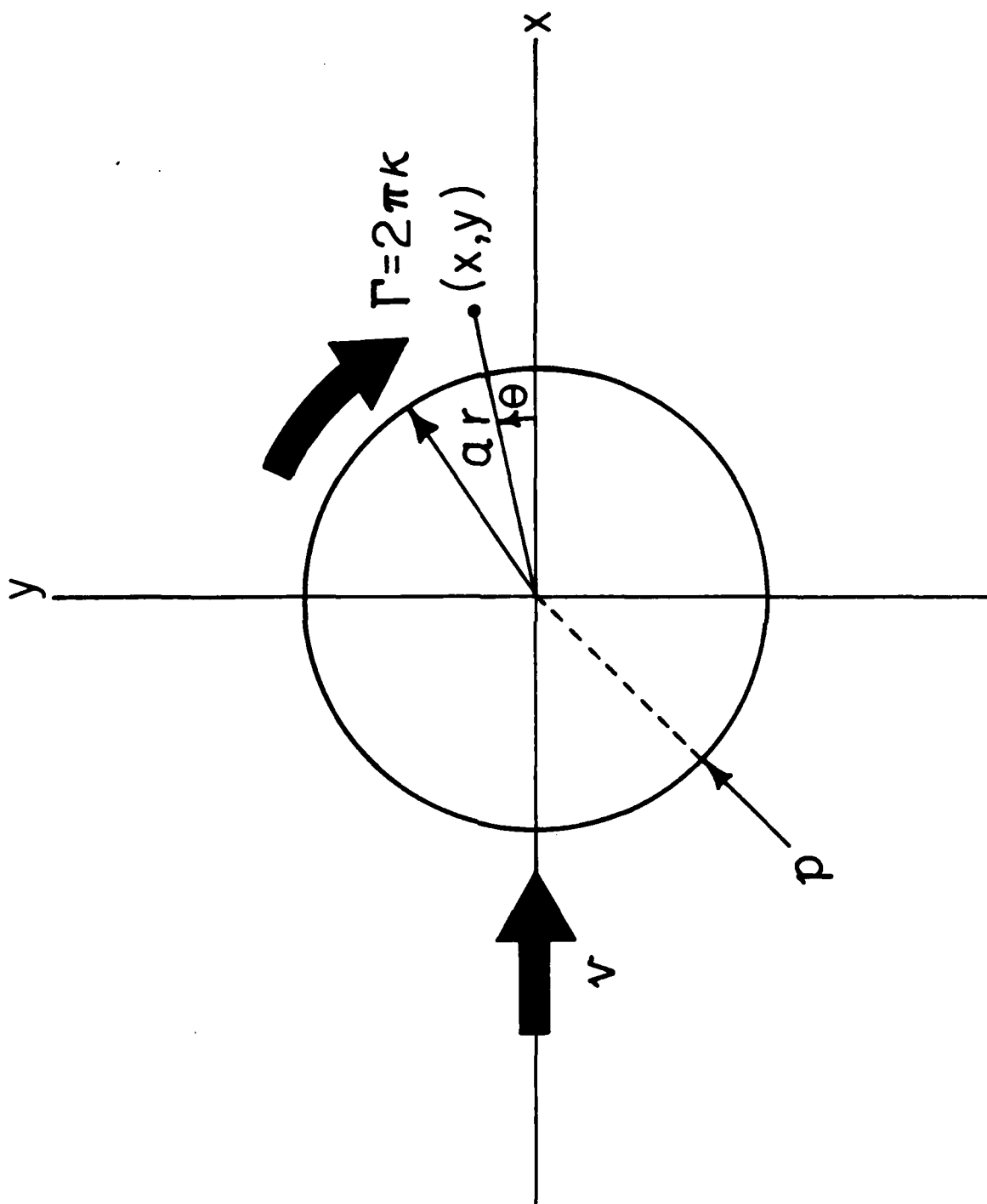


Figure 3: Circular Cylinder of Radius " a ", Lying Perpendicular to A Uniform Stream of Velocity V , and Exposed to a Circulation, Γ , of Strength κ , such that $\Gamma = 2\pi\kappa$.

$$\frac{dw}{dz} = - \left\{ V \left[1 - \frac{a^2}{z^2} \right] + i\kappa \frac{a}{az} \right\}$$

Thus, neglecting compressibility effects, $\vec{F} = - \frac{i\rho}{2} \left\{ V - \frac{a^2 V}{z^2} + \frac{i\kappa}{z} \right\}^2 dz$ (8)

Equation (8) is a complex integral to be taken around the contour of the cylinder. The integrand can be expanded to give:

$$V^2 + \frac{2iV\kappa}{z} - \frac{2a^2 V^2}{z^2} - \frac{\kappa^2}{z^2} - \frac{2ia^2 V\kappa}{z^3} + \frac{a^4 V^2}{z^4}$$

which is a specific form of the more generalized power series expansion:

$$f(z) = \sum_{n=-\infty}^{\infty} a_n (z - z_0)^n, \text{ where,}$$

$$a_n = \frac{1}{2\pi i} \oint \frac{f(\zeta) d\zeta}{(\zeta - z_0)^{n+1}}. \text{ In this case, } z_0 = 0, \text{ and } -4 \leq n \leq 0, \text{ with:}$$

$$a_0 = V^2$$

$$a_{-1} = \frac{1}{2\pi i} \oint f(\zeta) d\zeta = \text{sum of residues inside the contour} = 2iV\kappa$$

$$a_{-2} = -(2a^2 V^2 + \kappa^2)$$

$$a_{-3} = -2ia^2 V\kappa \text{ and,}$$

$$a_{-4} = a^4 V^2$$

Thus, $\oint f(z) dz = 2\pi i a_{-1} = 2\pi i (2iV\kappa)$, and so:

$$\vec{F} = - \frac{i\rho}{2} (2\pi i) (2iV\kappa) = 2i\rho\pi V\kappa$$

or, $\vec{F} = F_x + iF_y = 0 + i(2\rho\pi V\kappa)$. Finally, then:

$$F_x = 0, \text{ and}$$

$$F_y = \Gamma\rho V$$

(9)

Note the absence of a drag force, F_x , because the flow is initially considered to be irrotational. Furthermore, note that the "lift" force, F_y , depends on the circulation, Γ , about the cylinder. This circulation may be described in terms of the vortex-shedding characteristics of the double-cylinder configuration as follows: consider a point P located at coordinate $z_0 = x_0 + iy_0$ as shown in Figure 4 relative to the Row 1 vortices shed as illustrated in Figure 2. The velocity at point P due to any vortex, say Q, in row 1, may be obtained from the complex potential function for that vortex filament of strength κ_1 :

$$w = -i\kappa_1 \log(z - z_0) \quad (10)$$

where $(z - z_0) = re^{i\theta}$ defines the location (z) of the vortex relative to arbitrary point P(x_0, y_0) in the x-y plane. The negative sign in equation (10) indicates that the circulation around the filament is clockwise as shown in the Figures. From equation (10), we may write:

$$w = -i\kappa_1 \log(re^{i\theta}) = -i\kappa_1 [\log r + i\theta] = \phi + i\psi.$$

$$\text{Thus, } \phi = \kappa_1 \theta \text{ and } \psi = -\kappa_1 \log r,$$

$$\text{from which: } v_r = -\frac{\partial \phi}{\partial r} = 0 = -\frac{\partial \psi}{\partial \theta} \frac{1}{r} \quad (11)$$

$$v_\theta = -\frac{1}{r} \frac{\partial \phi}{\partial \theta} = -\frac{\kappa_1}{r} = \frac{\partial \psi}{\partial r}$$

and so it is observed that the direction of motion at P due to the vortex at Q is at right angles to the line QP or r (since $v_r = 0$), with speed κ_1/r , in the sense given by the rotation of the vortex at Q (hence the negative sign in the equation for v_θ). We may rewrite the equation for v_θ as:

$$v_\theta = v_p = -\frac{1}{r} \Gamma_1 / 2\pi \quad (12)$$

where $\Gamma_1 = 2\pi\kappa_1$ is the circulation of each vortex in row 1. If we now examine a "mirror" vortex located at the corresponding point Q' in row 1, it is noted that its effect at P is to induce a y-velocity component that cancels the one induced by the vortex at Q, and an x-velocity component that doubles the one already there due to the vortex at Q. Hence, the net velocity at P due to vortices at Q and Q' is in the negative x-direction and has magnitude:

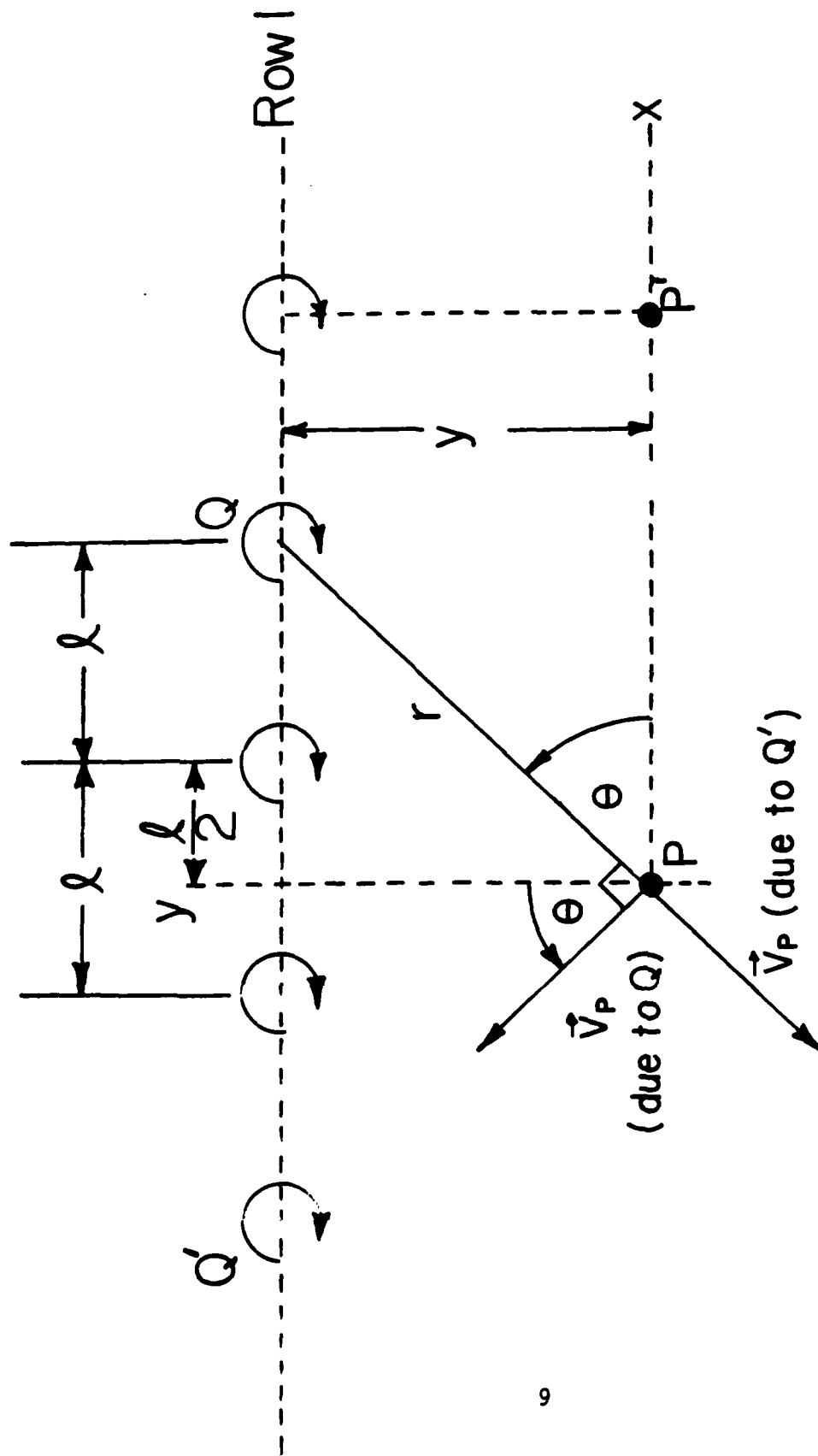


Figure 4: Velocity Induced at an Arbitrary Point, P , due to the Vortex Stream Generated in Row 1 Isolated from Figure 2.

$$\begin{aligned}
v_x &= -\frac{\Gamma_1}{2\pi} \frac{1}{r} (2) \sin\theta \\
&= -\frac{\Gamma_1}{2\pi} 2 \frac{r \sin\theta}{r^2} = -\frac{\Gamma_1}{\pi} \frac{y}{y^2 + \frac{9\ell^2}{4}}.
\end{aligned}$$

Generalizing the above discussion to any n 'th pair of vortices in row 1, we may write: $r^2 = (n\ell - \frac{\ell}{2})^2 + y^2$, and summing the effects of all the vortices in the row, we conclude that the velocity induced at P by the vortex stream in row 1 is:

$$\begin{aligned}
v_x &= \sum_{n=1}^{\infty} -\frac{\Gamma_1}{2\pi} 2 \frac{y}{(n\ell - \frac{\ell}{2})^2 + y^2} = -\sum_{n=1}^{\infty} \frac{\Gamma_1}{\pi\ell^2} \frac{y}{(n - \frac{1}{2})^2 + \frac{y^2}{\ell^2}} \\
&= -\frac{\Gamma_1}{2\ell} \frac{8y}{\pi\ell} \sum_{n=1}^{\infty} \frac{1}{(2n-1)^2 + \frac{4y^2}{\ell^2}} \quad \text{or,} \tag{13}
\end{aligned}$$

$$v_x = -\frac{\Gamma_1}{2\ell} \tanh \frac{\pi y}{\ell}$$

$$\text{where: } \frac{8y}{\pi\ell} \sum_{n=1}^{\infty} \frac{1}{(2n-1)^2 + \frac{4y^2}{\ell^2}} = \tanh\left(\frac{\pi}{2} \frac{2y}{\ell}\right)$$

(Gradshteyn and Ryzhik, 1965, page 36). Performing a similar analysis for a point P' located as shown in Figure 4, one obtains (Landweber, 1942):

$$v_{P'} = -\frac{\Gamma}{2\ell} \coth \frac{\pi y}{\ell} \tag{14}$$

Using equations (13) and (14), one can now write relationships for the velocity of vortices in any row of the street shown in Figure 2E. That is, a vortex in row 4 is travelling with a speed induced by the vortices in rows 1, 2, and 3. Hence:

$$\begin{aligned}
v_4 = v_1 &= -\frac{\Gamma_2}{2\ell} \tanh \frac{\pi h}{\ell} + \frac{\Gamma_2}{2\ell} \tanh \frac{(h+k)\pi}{\ell} \\
&\quad - \frac{\Gamma_1}{2\ell} \coth \frac{\pi(2h+k)}{\ell}
\end{aligned} \tag{15}$$

where Γ_2 is the circulation of each vortex in rows 2 and 3. Also, a vortex

in row 3, is travelling with a speed induced by the vortices in rows 1, 2, and 4. Hence:

$$v_3 = v_2 = -\frac{\Gamma_1}{2\ell} \tanh \frac{\pi h}{\ell} + \frac{\Gamma_2}{2\ell} \coth \frac{\pi k}{\ell} - \frac{\Gamma_1}{2\ell} \tanh \frac{\pi(k+h)}{\ell} \quad (16)$$

Examination of equations (15) and (16) clearly reveals that Γ_1 and Γ_2 could be calculated if we could say something about $v_1, v_2, v_3, v_4, \ell, h,$ and k . From stability considerations we do know that $v_1 = v_2 = v_3 = v_4$, but more information must be obtained. This can be achieved most conveniently by performing a series of relevant and carefully designed experiments. That is the subject of the section which follows. But before proceeding, it is of interest to use some related experimental data acquired by Landweber quite a long time ago. From his studies, Landweber (1942) suggested that the following are reasonable values for the parameters in equations (15) and (16): for small b , ($0 < b < .125a$), and for steady turbulent flow,

$$\frac{h}{k} = 1, \quad \ell = \pi h, \quad v_1 = v_2 = v_3 = v_4 = \frac{V}{4}$$

and $h = (1.3)2a$.

Substituting into (15):

$$v = \frac{1}{\pi(1.3)(2)(2a)} [-\Gamma_2 \tanh(1) + \Gamma_2 \tanh(2) - \Gamma_1 \coth(3)]$$

thus, $5.2\pi av = -.7616\Gamma_2 + .9640\Gamma_2 - 1.0050\Gamma_1.$

Substituting into (16):

$$v = \frac{1}{2\pi(1.3)2a} [-\Gamma_1 \tanh(1) + \Gamma_2 \coth(1) - \Gamma_1 \tanh(2)]$$

thus, $5.2\pi av = -.7616\Gamma_1 + 1.3130\Gamma_2 - .9640\Gamma_1.$

Rewriting:

$$.2024\Gamma_2 - 1.0050\Gamma_1 = 1.3\pi av$$

and, $1.3130\Gamma_2 - 1.7256\Gamma_1 = 1.3\pi av$

Solving simultaneously: $.2014\Gamma_2 - \Gamma_1 = 1.2935\pi aV$

$$\frac{.7609\Gamma_2 - \Gamma_1 = .7534\pi aV}{}$$

Subtract: $-.5595\Gamma_2 = .5401\pi aV$

Thus, $\Gamma_2 = -3.0327aV,$

(17)

and, $\Gamma_1 = -4.6745aV,$

where, in the steady state, Γ_2 is the maximum circulation in rows 2 and 3 driving the cylinders apart and Γ_1 is the maximum circulation in rows 1 and 4 driving the cylinders together. The negative sign is appropriate for rows 1 and 3, while it changes to a positive sign for rows 2 and 4.

SECTION IV

CALCULATION OF OSCILLATING LATERAL FORCES

At this point we have some estimate of the information necessary to evaluate equation (9) in order to determine the forces which cause the cylinders to oscillate after they have separated a small amount. To be consistent with an earlier report (Schneck, 1979) it is assumed that the radius of the cylinder is 1.5 inches (characteristic of the human forearm) and it has a length of one foot. Furthermore, an ejection taking place at an altitude of 10,000 feet is considered, where

$\frac{\rho}{\rho_0} = 0.7385$, $\rho_0 = 0.002378$ slug/ft³ and c , the local speed of sound is 1,078 ft/sec. Thus,

$$F_y = \Gamma \left(\frac{\rho}{\rho_0} \right) \rho_0 \frac{V}{c} = 1.8931 \Gamma M \sin \alpha \quad (18)$$

where: $V = U_0 \sin \alpha$ = magnitude of the cross-flow velocity,

U_0 = magnitude of free-stream air flow velocity,

α = angle of attack between cylinder axis and direction of air flow velocity, and,

$M = U_0/c$ = Mach number of the flow.

Substituting Γ_2 from equation (17) into equation (18), with $a = 1.5$ inches, we obtain the maximum force driving the cylinders apart, which is:

$$F_2 = 1.8931 \Gamma_2 M \sin \alpha = 1.8931 (3.0327) \frac{1.5}{12} \frac{U_o \sin \alpha}{c} (1078) M \sin \alpha, \text{ or,}$$

$$F_2 = 773.6 M^2 \sin^2 \alpha \quad (19)$$

Similarly, substituting Γ_1 from equation (17) into equation (18) we obtain the maximum force driving the cylinders together, which is:

$$F_1 = 1.8931 [4.6745 \left(\frac{1.5}{12} \right) \frac{U_o \sin \alpha}{c} (1078) M \sin \alpha], \text{ or,}$$

$$F_1 = 1192.4 M^2 \sin^2 \alpha \quad (20)$$

The time-course of aerodynamic forces that prevail some time following the onset of windblast thus oscillates between the extremes defined by equations (19) and (20). The frequency, m , of such oscillation depends on the vortex shedding frequency, which is usually expressed in terms of the dimensionless Strouhal number:

$$S = \frac{m(2a)}{V} \quad (21)$$

Thus, $m = \frac{SV}{2a}$. But, this vortex shedding frequency can also be written in terms of the number of times per second that vortices in a given row, j , pass any particular point, i.e.,

$$m = \frac{V - v_j}{\ell} \quad (22)$$

Writing, as before, $v_j \approx \frac{V}{4}$, $V = U_o \sin \alpha$, $\ell = \pi h$, $h = 2.6a$, $M = \frac{U_o}{c}$, $a = 1.5$ inches, and $c = 1078$ ft/sec, equation (22) reduces to:

$$m = \frac{V - \frac{V}{4}}{\pi h} = \frac{\frac{3}{4} U_o \sin \alpha}{\pi (2.6)a} = \frac{\frac{3}{4} M (1078) \sin \alpha}{\pi (2.6) \frac{(1.5)}{12}}, \text{ or,}$$

$$m = 791.86 M \sin \alpha \text{ per second} \quad (23)$$

with a corresponding Strouhal number:

$$S = \frac{\frac{3}{4} V (2a)}{\pi (2.6) a V} = .1836 \text{ characterizing the flow.}$$

Now write: $\omega = 2\pi m = \text{circular frequency}$

$$A = \frac{F_2 + F_1}{2} = \text{amplitude of the oscillation}$$

$$A_o = F_2 - A = A - F_1 = \text{mean of the oscillation.}$$

Then, from equations (19), (20) and (23):

$$\omega = 4975.38 M \sin \alpha,$$

$$A = 983 M^2 \sin^2 \alpha, \text{ and}$$

$$A_o = -209.4 M^2 \sin^2 \alpha$$

so that the oscillating forces generated by the double vortex street described earlier can be defined by the equations:

$$\begin{aligned} t > 0^+ \quad (\text{steady state}) \quad F(t) &= A_o + A \cos \omega t \\ &= M^2 \sin^2 \alpha [-209.4 + 983 \cos(4975.4 M \sin \alpha) t] \end{aligned} \quad (24)$$

$$t = 0 \quad F(0) = 1148 M^2 \sin^2 \alpha \quad (25)$$

where the negative sign corresponds to the cylinders being driven together and the positive sign represents the cylinders being driven apart.

Now, it is reasonable to expect that the transition from equation (25)

at $t = 0$ to equation (24) in the steady state for $t > 0^+$ does not occur instantaneously or discontinuously, but rather, is characterized by some time constant, τ . Due to the physics of the process, however, one can surmise further that τ is very small, perhaps on the order of one-quarter or less of the period defined by the reciprocal of equation (23). Such a small time constant would cause the transient stage of the flow adjustment to last effectively one complete cycle, since after a lapse of time equal to four time constants the transient components of the process will have decayed to

some 2% of their initial value. Thus, let $\tau = \frac{1/4}{791.86 M \sin \alpha}$ and combine

equations (24) and (25) in the form:

$$F(t) = M^2 \sin^2 \alpha \left\{ 374.4 e^{-\frac{t}{\tau}} - 209.4 + 983 \cos[4975.4 M \sin \alpha] t \right\} \quad (26)$$

observe that equation (26) reduces to equation (25) for $t = 0$, and equation (26) reduces to equation (24) as $t \rightarrow \infty$. In a practical sense, however, the leading term of equation (26) is down to 2% of its initial value by the time $t = 4\tau$, which is after one complete cycle has transpired.

Figure 5 shows equation (26) plotted with $M \sin \alpha$, acting as a parameter. Essentially, $M \sin \alpha$ may be redefined by some new variable, say M_c , repre-

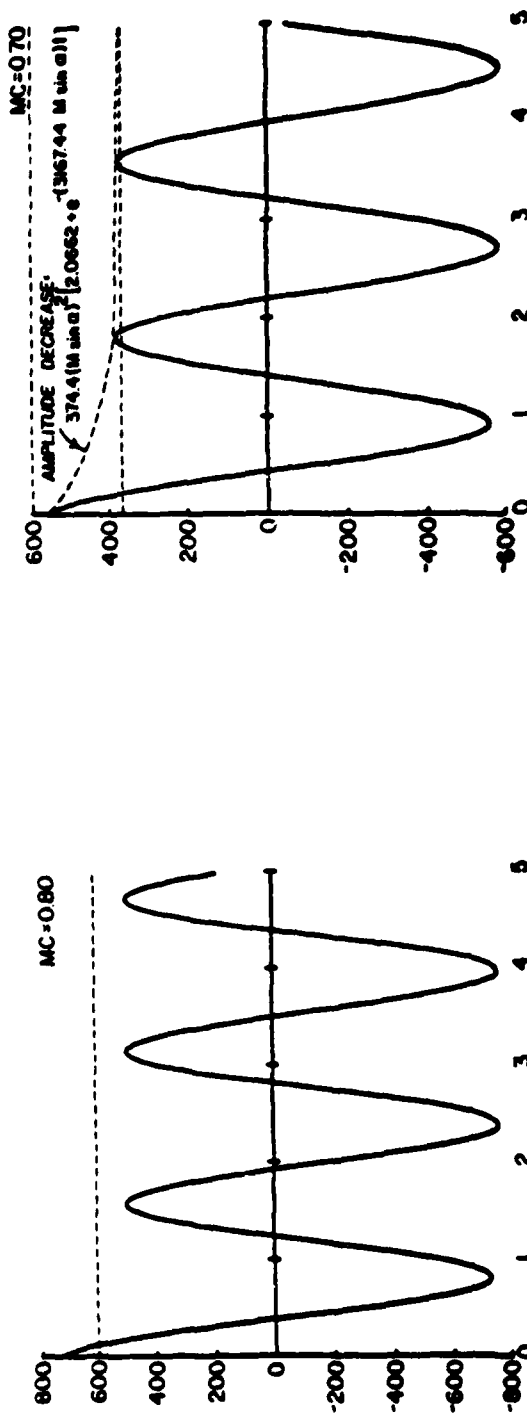
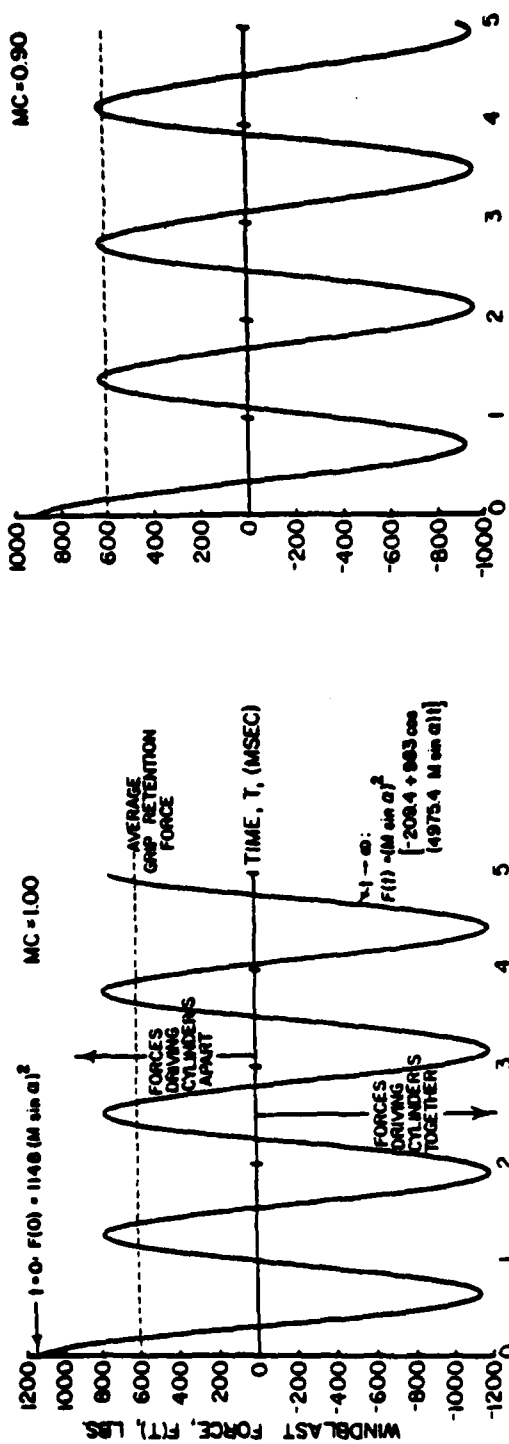


Figure 5: Oscillating Windblast Forces that Prevail at the Indicated Cross-Flow Mach Numbers, MC.

senting the cross-flow Mach number of the air passing over the limbs of the ejection seat occupant. Note that M_C may vary over different portions of the body that intercept the flow at different angles α .

Equation (25), valid at $t = 0$, (or, the limit of equation (26) as $t \rightarrow 0$) plots along the vertical axis at the origin of the coordinate system, and defines the limb-dislodging force that prevails for the situation depicted in Figure 1. Equation (24), (or, the limit of equation (26) as $t \rightarrow \infty$) then describes the oscillating lateral forces that are associated with the double vortex street pattern which develops after some time in accordance with the events illustrated in Figure 2 for $t > 0$. The parameter $M \sin \alpha$ is examined only for cross-flow Mach numbers $M_C \leq 1$, i.e., in the sub-and-early-transonic range.

Observe, first of all, that the frequency of the oscillating lateral forces increases linearly with M_C according to equation (23) (plotted in

Figure 6), and that it becomes rather substantial at higher cross-flow Mach numbers. This may explain, in part, the observed and often harmful vibration which takes place between the head/neck of the pilot and the ejection seat head rest during higher-speed ejections. Even allowing for the inertial resistance of the mass of the head, it is likely that vibrations on the order

of 10^2 cycles per second may accompany ejections occurring above $M_C = 0.7$,

where the forces generated exceed the limits of musculo-skeletal resistance.

Writing:

$$F(t) = M_s a_s(t), \quad (27)$$

assuming a simple, unrestrained, two dimensional, rectilinear situation, one may estimate the kinematics of the ensuing motion of a body segment of mass M_s , subjected to the force distribution defined by equation (26). Thus,

$$a_s(t) = \frac{F(t)}{M_s} = \frac{M^2 \sin^2 \alpha}{M_s} \{ 374.4 e^{(-3167.44 t M \sin \alpha)} - 209.4 + 983 \cos[4975.4 M \sin \alpha] t \} \quad (28)$$

Integrate equation (28) to get velocity:

$$v_s(t) = \frac{M^2 \sin^2 \alpha}{M_s} \left\{ \frac{-.1182 e^{(-3167.44 t M \sin \alpha)}}{M \sin \alpha} - 209.4 t + \frac{.1976}{M \sin \alpha} \sin[4975.4 M \sin \alpha] t + C_1 \right\} \quad (29)$$

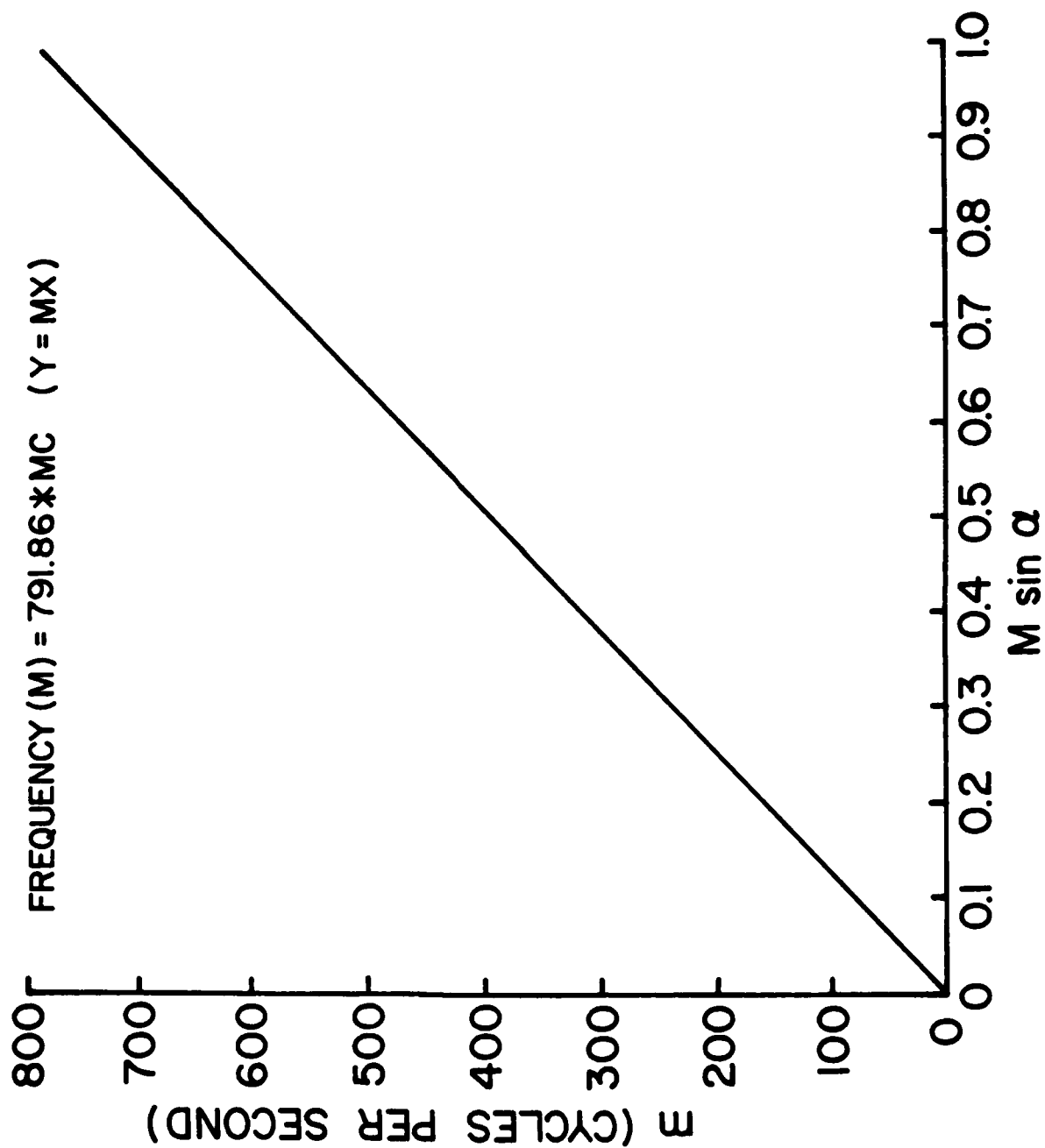


Figure 6: Frequency of the Oscillating Lateral Forces Illustrated in Figure 5, Plotted as a Function of the Cross-Flow Mach Number, MC .

where: $C_1 = \frac{.1182}{M \sin \alpha}$ if it is assumed that $v_s(0) = 0$. Going one step further, integrate equation (29) to get corresponding limb displacement:

$$\delta_s(t) = \frac{M^2 \sin^2 \alpha}{M_s} \left\{ \frac{.3732 \times 10^{-4} e^{(-3167.44t M \sin \alpha)}}{M^2 \sin^2 \alpha} - 104.7t^2 \right. \\ \left. - \frac{.3971 \times 10^{-4}}{M^2 \sin^2 \alpha} \cos[4975.4 M \sin \alpha]t + \frac{.1182t}{M \sin \alpha} + C_2 \right\} \quad (30)$$

where: $C_2 = -\frac{.3732 \times 10^{-4}}{M^2 \sin^2 \alpha} + \frac{.3971 \times 10^{-4}}{M^2 \sin^2 \alpha}$ if it is further assumed that $\delta_s(0) = 0$.

Writing $t = \frac{t}{\tau}$, where $\tau = \frac{(3.1571 \times 10^{-4})}{M \sin \alpha}$, equation (30) reduces to:

$$\delta_s(t) = \frac{1}{M_s} \left\{ .3732 \times 10^{-4} e^{-\frac{t}{\tau}} - .1044 \times 10^{-4} \left(\frac{t}{\tau}\right)^2 \right. \\ \left. - .3971 \times 10^{-4} \cos(1.5708)\frac{t}{\tau} + .3732 \times 10^{-4} \frac{t}{\tau} \right. \\ \left. + .0239 \times 10^{-4} \right\},$$

or,

$$\delta_s(\eta) = \frac{10^{-4}}{M_s} \left\{ .3732 e^{-\eta} - .3971 \cos\left(\frac{\pi}{2} \eta\right) \right. \\ \left. - .1044 \eta^2 + .3732 \eta + .0239 \right\} \quad (31)$$

where: $\eta = \frac{t}{\tau}$. Equation (31) defines an exponentially decaying cosine wave

super-imposed on a parabola represented by the last three terms. One com-

plete cycle, (4 time constants) is shown in Figure 7, where $\delta_s(\eta) M_s 10^4$ is

plotted against η for $0 \leq \eta \leq 4$. Observe that during this early phase of the ejection process, the tendency for the displacement of a limb-segment is directed away from a restraining surface, i.e., $\delta_s(\eta)$ is positive at least up

to $\eta = 3$. While the actual displacements predicted by equation (31) are small (typically on the order of 0.20 mm), our concern in this simple example is less with specific numbers than with physical trends. That is, the fact that $\delta_s(\eta)$ is initially positive is significant because when the

peripheral limbs (arms and lower legs) become separated from the torso area

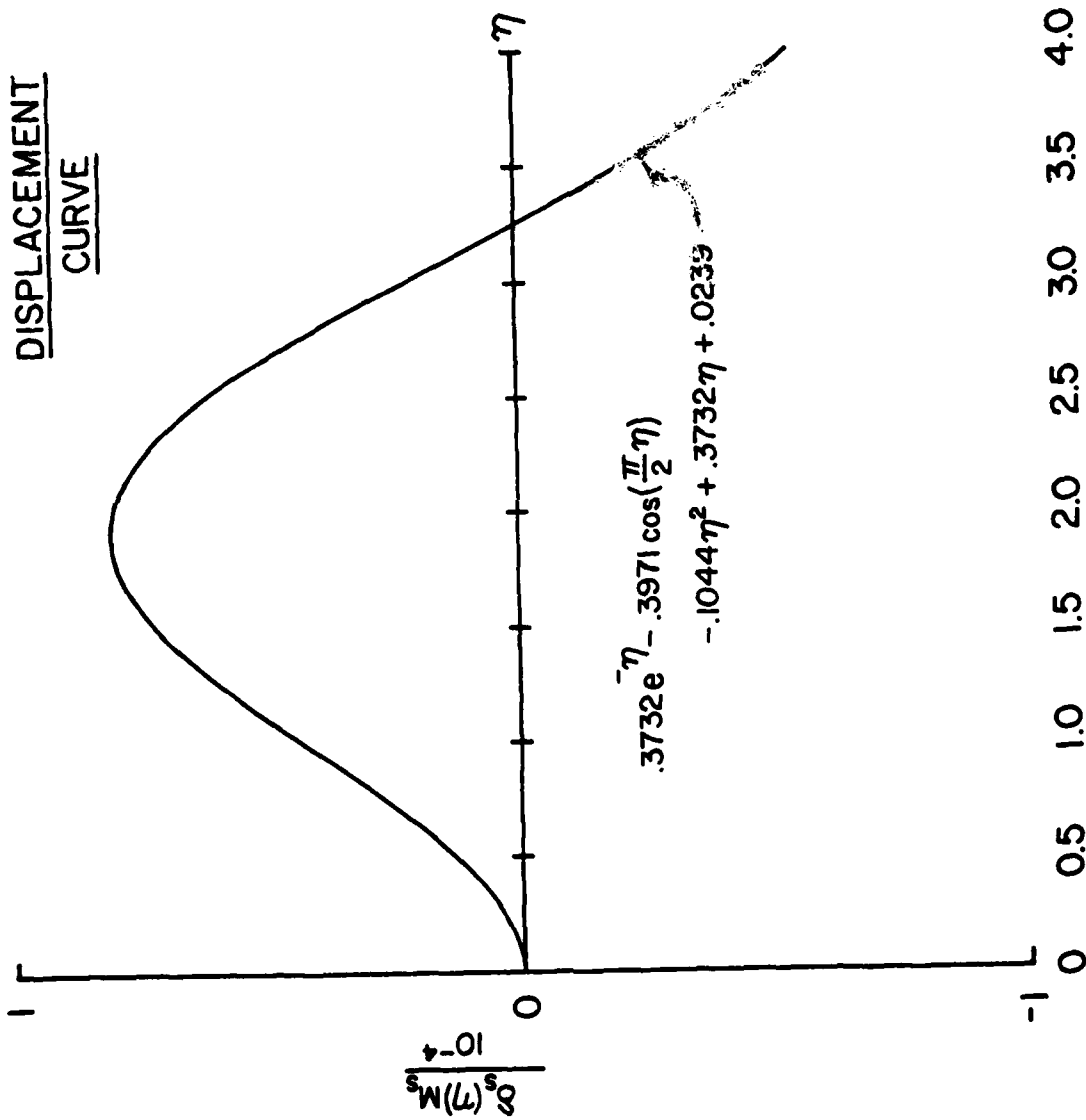


Figure 7: Limb Displacement During the Initial Stages of Aircraft Ejection

in a situation where the seat provides little or no restraint, drag forces are more likely to cause an uncontrolled flail, rather than a simple lateral vibration (such as might occur between the head and head rest). Moreover, this theory suggests what the evidence has revealed to be the case, i.e., that contrary to what one might suspect a priori, there is a violent forward head rotation (away from the restraining head rest) at the initial instant of ejection - with a strong likelihood of incipient neck injury. Of course, musculo-skeletal resistance has not been taken into account to this point in the analysis; but Figure 5 further reveals the likelihood that the oscillating forces generated beyond $M_Q = 0.70$ exceed at least the average grip

retention force reported by Horner and Hawker (1973) for significant portions of the pulse cycle. It thus follows that flail seems somewhat inevitable at these higher Mach numbers and angles of attack, regardless of the pilot's efforts to "hold on." In any case, equations (28)-(31) are only simplifications intended to reveal a trend. More exact kinematic information can be obtained by exercising the Aerospace Medical Research Laboratory's Articulated Total Body Model (ATB) with equation (26) providing input data relative to the aerodynamic loading that prevails during a given ejection situation. In fact, even equation (26) is an approximation (although realistic) based on the results of Landweber (1942). It is thus desirable to back up still further to equations (9), (15) and (16) and to accumulate somewhat more relevant experimental information concerning the wake that develops downstream of a double-cylinder configuration. To do so, we shall exploit the principle of the Hydraulic Analogy as described below.

SECTION V

PRINCIPLE OF THE HYDRAULIC ANALOGY

The idea behind the hydraulic analogy concept is to be able to deduce what goes on in a two-dimensional high-speed compressible flow (e.g., aircraft ejections) from measurements made in an incompressible, open-channel flow. The analogy itself is based on the correspondence between pressure waves in a compressible gas and gravity waves on the free surface of a liquid (see, for example, Shapiro, 1949). For example, consider the flow of a liquid in an open channel of arbitrary cross-section as shown in Figure 8. Here, the equation of the cross-section is taken to be a power law of the form:

$$x(y) = By^\beta, \quad (32)$$

which is assumed to be uniform in the x-direction (coming out of the paper). Let the maximum water level at some arbitrary x-section be ξ_1 , corresponding to a surface channel half-width g_1 . Then the fluid filled cross-sectional area, A_1 at this x-station is:

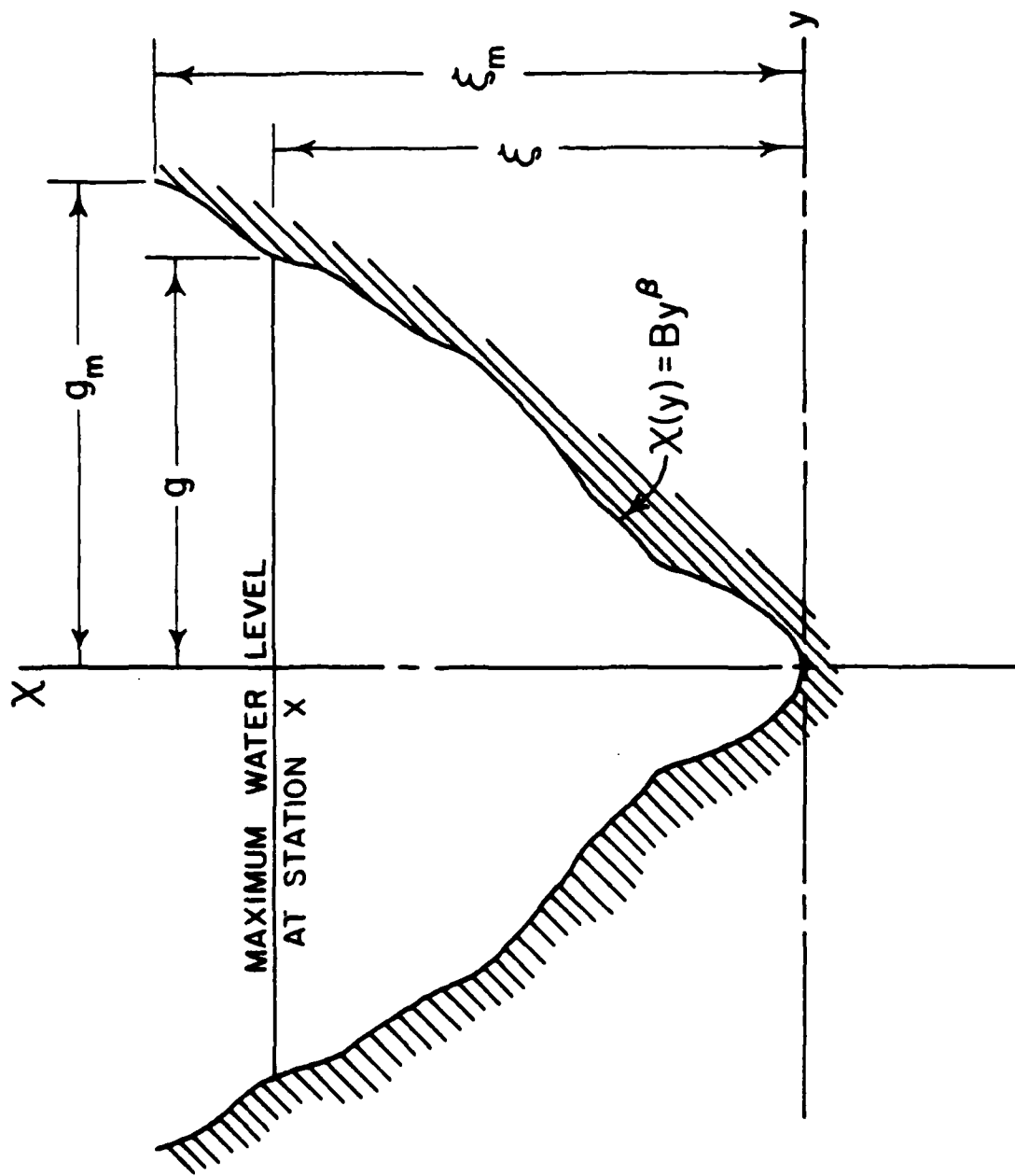


Figure 8: Open Water Channel of Arbitrary Cross-Section

$$\begin{aligned}
A_1 &= 2 \int_0^{g_1} [\xi_1 - \chi(y)] dy \\
&= 2 \int_0^{g_1} \xi_1 dy - 2 \int_0^{g_1} B y^\beta dy \\
&= 2 \xi_1 y \Big|_0^{g_1} - \frac{2 B y^{\beta+1}}{\beta+1} \Big|_0^{g_1} \\
&= 2 \xi_1 g_1 - 2 \left(\frac{\xi_1}{\beta} \right) \frac{g_1^\beta g_1}{g_1} \\
&= \frac{2 \xi_1 g_1^\beta + 2 \xi_1 g_1 - 2 \xi_1 g_1}{\beta+1} = \frac{2 \xi_1 \beta \xi_1^{1/\beta}}{(\beta+1) B^{1/\beta}}
\end{aligned}$$

$$\text{therefore } A_1 = \frac{\beta}{\beta+1} \frac{2}{B^{1/\beta}} \xi_1 \frac{\beta+1}{\beta} . \quad (33)$$

Now, due to the existence of gravity wave motion, the fluid-filled cross-sectional area at some other x-station will be different from A_1 , say,

$$A_2 = \frac{\beta}{\beta+1} \frac{2}{B^{1/\beta}} \xi_2 \frac{\beta+1}{\beta} . \quad (34)$$

But, for an incompressible fluid, continuity requires that:

$$A_1 V_1 = A_2 V_2 \quad (35)$$

where V_1 and V_2 are the mean flow velocities at stations 1 and 2, respectively. Thus,

$$\begin{aligned}
\frac{V_2}{V_1} &= \frac{A_1}{A_2} = \frac{\beta}{\beta+1} \frac{2}{B^{1/\beta}} \xi_1 \frac{\beta+1}{\beta} \frac{\beta+1}{\beta} \frac{B^{1/\beta}}{2} \xi_2^{-\frac{\beta+1}{\beta}} , \text{ or,} \\
\frac{V_2}{V_1} &= \left(\frac{\xi_1}{\xi_2} \right)^{\frac{\beta+1}{\beta}} \quad (36)
\end{aligned}$$

In order to have equation (36) be analogous to a corresponding compressible flow situation, we note that the continuity equation for the two-dimensional

steady flow of a compressible fluid through a region of constant cross-section is:

$$\rho_1 V_1 = \rho_2 V_2, \text{ or,} \quad (37)$$

$$\frac{V_2}{V_1} = \frac{\rho_1}{\rho_2} \quad (38)$$

Thus, in the hydraulic analogy, equating equations (38) and (36) yields:

$$\left(\frac{\xi_1}{\xi_2}\right)^{\frac{\beta+1}{\beta}} = \frac{\rho_1}{\rho_2} \quad (39)$$

so that depth changes due to wave motion in an incompressible open channel flow are proportional in the analogy to density changes due to wave motion in a compressible gas-dynamic flow. Carrying the analogy one step further, consider Bernoulli's equation applied on the free surface of the open channel flow:

$$\frac{p_1}{\rho g_c} + \frac{V_1^2}{2g_c} + \xi_1 = \frac{p_2}{\rho g_c} + \frac{V_2^2}{2g_c} + \xi_2 = \xi_0 \quad (40)$$

An "average" form of equation (40) may be written more generally for a channel of arbitrary cross-section by introducing the concept of the hydraulic mean depth, ξ^* . This is essentially a modified parameter that accounts for the fact that the cross-section of the open channel may not be rectangular. The hydraulic Mean Depth is defined as the ratio of the fluid filled cross-sectional area, A , at any x -station, to the wetted perimeter, P_w at that same station. The latter is defined as:

$$P_w = 2 \int_0^g \sqrt{1 + \left(\frac{dx}{dy}\right)^2} dy \quad (41)$$

In order to evaluate equation (41), we first make some observations concerning the derivative $\left(\frac{dx}{dy}\right)$. That is, let $\sigma = \frac{x(y)}{\xi_m}$ and $\epsilon = \frac{y}{g_m}$. Then, $\frac{d}{dy} = \frac{d}{d\epsilon} \frac{d\epsilon}{dy} = \frac{1}{g_m} \frac{d}{d\epsilon}$, so, $\frac{dx}{dy} = \frac{\xi_m}{g_m} \frac{d\sigma}{d\epsilon} = \text{order } \left(\frac{\xi_m}{g_m}\right)$. For a shallow (small ξ_m) wide (large g_m) channel, then, where $\frac{\xi_m}{g_m} \ll 1$, one may certainly conclude that $\left(\frac{dx}{dy}\right)^2 = O\left(\frac{\xi_m}{g_m}\right)^2$ is negligible compared with unity. The neglect of this derivative in determining P_w is thus a reasonable approximation, so we may

write, for a wide, shallow channel,

$$P_w = 2 \int_0^g dy = 2y \Big|_0^g = 2g \quad (42)$$

From equation (33), $A = \frac{2\xi g \beta}{\beta+1}$. The hydraulic mean depth at any x-station can finally be expressed as:

$$\xi^* = \frac{A}{P_w} = \frac{2\xi g \beta}{(\beta+1)2g} = \frac{\beta}{\beta+1} \xi, \quad (43)$$

where ξ is the corresponding maximum fluid depth at that station.

Assuming the liquid surface is open to the atmosphere, we can take $p_1 = p_2 = 0$ in equation (40). Thus, utilizing equation (43), Bernoulli's equation for any point, x, may be written:

$$\frac{v^2}{2g_c} + \frac{\beta+1}{\beta} \xi^* = \frac{\beta+1}{\beta} \xi_o^* \quad (44)$$

Dividing equation (44) by ξ^* , multiplying by $\frac{\beta}{\beta+1}$, and defining the Froude number as $Fr = \sqrt{\frac{v^2}{g_c \xi^*}}$, one obtains:

$$\frac{\beta}{\beta+1} \frac{(Fr)^2}{2} + 1 = \frac{\xi_o^*}{\xi^*} = \frac{\frac{\beta}{\beta+1} \xi_o}{\frac{\beta}{\beta+1} \xi} = \frac{\xi_o}{\xi} \quad (45)$$

Now apply the energy equation to a compressible fluid: Heat Added + Work Done on The Fluid = Increase of Fluid Energy. Assuming the fluid does no work, the work done on the fluid (per unit mass) is: $\frac{p_1}{\rho_1} - \frac{p_2}{\rho_2}$. Neglecting field forces, the corresponding increase of fluid energy per unit mass is: $(e_2 + \frac{1}{2} v_2^2) - (e_1 + \frac{1}{2} v_1^2)$, where $e_{1,2}$ represents internal energy. Finally, considering an adiabatic process (heat added = 0), the energy equation may be written:

$$\left(\frac{p_1}{\rho_1} + e_1\right) - \left(\frac{p_2}{\rho_2} + e_2\right) = \frac{1}{2}(v_2^2 - v_1^2) \quad (46)$$

and, defining enthalpy $H = \frac{p}{\rho} + e$,

$$H_1 + \frac{v_1^2}{2} = H_2 + \frac{v_2^2}{2} = H_o = H + \frac{v^2}{2} \quad (47)$$

Now, for a perfect gas, (thermally and calorically), $H = c_p T$. Furthermore, the local speed of sound, c , can be expressed in terms of temperature T by the relation $c^2 = \gamma RT$, where $R = c_p - c_v$ is the gas constant for air and $\gamma = \frac{c_p}{c_v}$. Thus, $c^2 = \frac{HR}{c_v} = \frac{H(c_p - c_v)}{c_v} = H(\gamma - 1)$, and equation (47) becomes:

$$\frac{c^2}{\gamma - 1} + \frac{v^2}{2} = \frac{c_o^2}{\gamma - 1} \quad (48)$$

Dividing equation (48) by c^2 and defining the Mach Number as $M = \frac{v}{c}$, one obtains:

$$\frac{1}{\gamma - 1} + \frac{M^2}{2} = \frac{1}{\gamma - 1} \frac{\gamma RT_o}{\gamma RT}, \text{ or,} \\ (\gamma - 1) \frac{M^2}{2} + 1 = \frac{T_o}{T} \quad (49)$$

Note that equation (49) would be identical to equation (45) if the Mach number were equal to the Froude number, if the temperature ratio $\frac{T_o}{T}$ corresponded to the depth ratio $\frac{\xi_o}{\xi}$, and if the following relationship held:

$$\frac{\beta}{\beta + 1} = (\gamma - 1). \quad (50)$$

It thus follows that depth changes due to wave motion in an incompressible open channel flow are directly proportional to temperature changes due to wave motion in a compressible gas-dynamic flow; and that in the hydraulic analogy there is a one-to-one correspondence between the incompressible Froude number, which measures the importance of gravity in the wave motion, and the compressible Mach number, which measures the importance of fluid compressibility in the wave motion. To complete the analogy, we introduce the perfect gas relationship, $p = \rho RT$, to obtain, using equation (39),

$$\frac{p_o}{p} = \frac{\rho_o RT_o}{\rho RT} = \left(\frac{\xi_o}{\xi}\right)^{\frac{\beta+1}{\beta}} \left(\frac{\xi_o}{\xi}\right) = \left(\frac{\xi_o}{\xi}\right)^{\frac{2\beta+1}{\beta}}, \quad (51)$$

so that once again we note the correspondence between pressure waves in a compressible gas and gravity waves on the free surface of a liquid. It might be well at this point to review the assumptions which are inherent in the hydraulic analogy, and to summarize the results:

Assumptions: a) Bernoulli's equation (and to some extent, the continuity equation), as used here for an incompressible fluid, pre-supposes the existence of an isotropic, homogeneous, inviscid, Newtonian continuum, in a state of thermodynamic equilibrium, undergoing steady, essentially, one-dimensional flow in a rigid channel of uniform, constant cross-section, where gravity is the only body force, and where there is no heat transfer, no significant change in internal energy, no significant energy losses, and no work done on the fluid (by a pump, for example) or by the fluid (on a turbine or other device). b) The energy equation, as used here for a thermally and calorically perfect gas, also pre-supposes the existence of an isotropic, homogeneous, inviscid, Newtonian continuum, in a state of thermodynamic equilibrium, undergoing steady, essentially two-dimensional flow through a region of uniform cross-section, where gravity is the only body force, and where there is no heat transfer, no significant energy losses, and no work done by the fluid. c) The rigid channel is assumed to be wide, and to have a uniform, symmetric constant cross-section which can be defined by a power-law relationship and which is open to the atmosphere at its top. The fluid in the channel is further assumed to maintain a shallow, relatively constant (in the x-direction) depth and the effects of surface tension are neglected.

Over the years, many investigators have addressed themselves to the consequences and implications of this rather impressive list of assumptions as they relate to the validity of the hydraulic analogy (see, for example, Preiswerk, 1940, Ippen and Harleman, 1950, and Harleman and Crossley, 1952). Suffice it to say that the analogy is far from universally valid, especially in situations where the continuum assumption breaks down (rarefied gas dynamics in the upper atmosphere) or where there are substantial losses of energy (such as when shock waves form in supersonic flows). However, even in these extreme situations, "the water table has been strikingly successful in reproducing most qualitative aspects of high speed flows. It has the great advantages of simplicity, low cost, rapid operation, and gives the operator a chance to 'play' with various flow patterns. It is especially suitable for observing unsteady and transient flow patterns." (Shapiro, 1949). One might add that the water channel lends itself much more conveniently and cheaply to effective flow visualization techniques than does any other form of experimental procedure. Moreover, in the case of shock phenomena, the analogy can be corrected by replacing the gas-dynamic equations with appropriate shock relationships and the steady flow hydraulic equations with hydraulic jump equations.

In summary, "Despite the many questionable features of the analogue, the water channel is a valuable auxiliary tool which has the ability to shed light on problems of current importance in two-dimensional flow. It justifies itself through economy of time and effort and is useful for making qualitative studies and quantitative experiments of a comparative nature" (Shapiro, 1949).

With this in mind, table I has been prepared to highlight the essential features of the analogy which allows aerodynamic situations to be studied in open channel, shallow water models.

We call particular attention to the analogue relationship, equation (50), which establishes the cross-section geometry required of the open channel as a function of the specific heat ratio of the gas to be studied. Equation (50) is plotted in Figure 9, where it is observed that the curve is asymptotic to $\gamma = 2$ for $\beta \rightarrow \infty$. Rearranging equation (32) reveals that $\beta \rightarrow \infty$ corresponds to the condition:

$$\left[\frac{\chi(y)}{\xi_m} \right]^{1/\beta} = \frac{y}{g_m} = 1 \text{ for all } x > 0, \text{ or,}$$

as $\beta \rightarrow \infty$, $y = g_m = \text{constant}$ for all x bigger than zero. If $\left(\frac{y}{g_m}\right) < 1$, then $\left(\frac{y}{g_m}\right)^\beta \rightarrow 0$ as $\beta \rightarrow \infty$, so this condition only holds along the special line $\chi(y) = 0$. Thus, we have, for $\chi(y) = 0$, $\left(\frac{y}{g_m}\right) \leq 1$ and for $\chi(y) = \text{arbitrary}$, $\frac{y}{g_m} = 1$, which, together, define a channel of rectangular cross-section, having half-width g_m and arbitrary depth ξ_m . Note also that, for such a channel, $\xi = \xi^*$, as observed by letting $\beta \rightarrow \infty$ in equation (43). That is, the hydraulic mean depth for a shallow channel of rectangular cross-section is simply the same as the actual fluid depth at any x -station.

In most cases, the use of rectangular channels is convenient, but, of course, assumes the existence of a hypothetical perfect gas having a specific-heat ratio, γ , equal to 2. For most real gases, γ is more nearly in the range 1.2 to 1.5 (Streeter, 1961). Its value in air, for example, is 1.4, which corresponds to a channel having a cross-sectional contour given by:

$$\sigma = \frac{\chi(y)}{\xi_m} = \left(\frac{y}{g_m}\right)^{2/3} = \epsilon^{2/3} \quad (52)$$

Such a channel is illustrated in Figure 10, as are the corresponding cross-sections for $\gamma = 1.5$ (triangular contour, $\beta = 1$), $\gamma = 1.2$ ($\beta = \frac{1}{4}$) and $\gamma = 2$ (rectangular cross-section). Note that the triangular contour, which is reasonably convenient to design and build, provides a good approximation ($\gamma = 1.5$) to the analogy for aerodynamics ($\gamma = 1.4$). Fortunately, however, it turns out that the rectangular channel ($\gamma = 2.0$), which is even more convenient from the point of view of scaling the body models to be studied (Whicker, 1951), gives results that are quite acceptable for qualitative flow assessment. In fact, the errors thus introduced are not too serious in both the subsonic and in the supersonic regimes (Streeter, 1961) and they are less important than, for example, the boundary layer which develops on the bottom of the fluid stream, the viscosity, the thermal conductivity

TABLE I
THE HYDRAULIC ANALOGY

	HYDRAULIC SYSTEM	AERODYNAMIC SYSTEM
Continuity Equation	$AV = \text{Constant}$ $\left(\frac{\partial x}{\partial t}\right) + \frac{\partial(xv_x)}{\partial x} + \frac{\partial(xv_y)}{\partial y} = 0$	$\rho V = \text{Constant}$ $\left(\frac{\partial \rho}{\partial t}\right) + \frac{\partial(\rho v_x)}{\partial x} + \frac{\partial(\rho v_y)}{\partial y} = 0$
Energy Equation	$\frac{\beta+1}{\beta} \epsilon^* + \frac{v^2}{2g_c} = \frac{\beta+1}{\beta} \epsilon_0^*$	$\frac{\gamma T}{\gamma-1} + \frac{v^2}{2R} = \frac{\gamma T_0}{\gamma-1}$
Hydraulic Radius	$\epsilon^* = \frac{\beta}{\beta+1} \epsilon$	
Gravity Effect	$\text{Froude Number, } F^2 = \frac{v^2}{\epsilon^* g_c}$	
Compressibility Effect		$\text{Mach Number, } M = \frac{v}{c}$
Analogous Parameters	$\left(\frac{\epsilon_0}{\epsilon}\right)^{\frac{\beta+1}{\beta}}$	$\frac{p_0}{p}$
	$\left(\frac{\epsilon_0}{\epsilon}\right)$	$\frac{T_0}{T}$
	$\left(\frac{\epsilon_0}{\epsilon}\right)^{\frac{2\beta+1}{\beta}}$	$\frac{p_0}{p}$
	F	M
Channel Equation	$x(y) = By^\beta = \epsilon_m \left(\frac{y}{g_m}\right)^\beta$	
Analog Relationship	$\frac{\beta}{\beta+1} = \gamma - 1$	

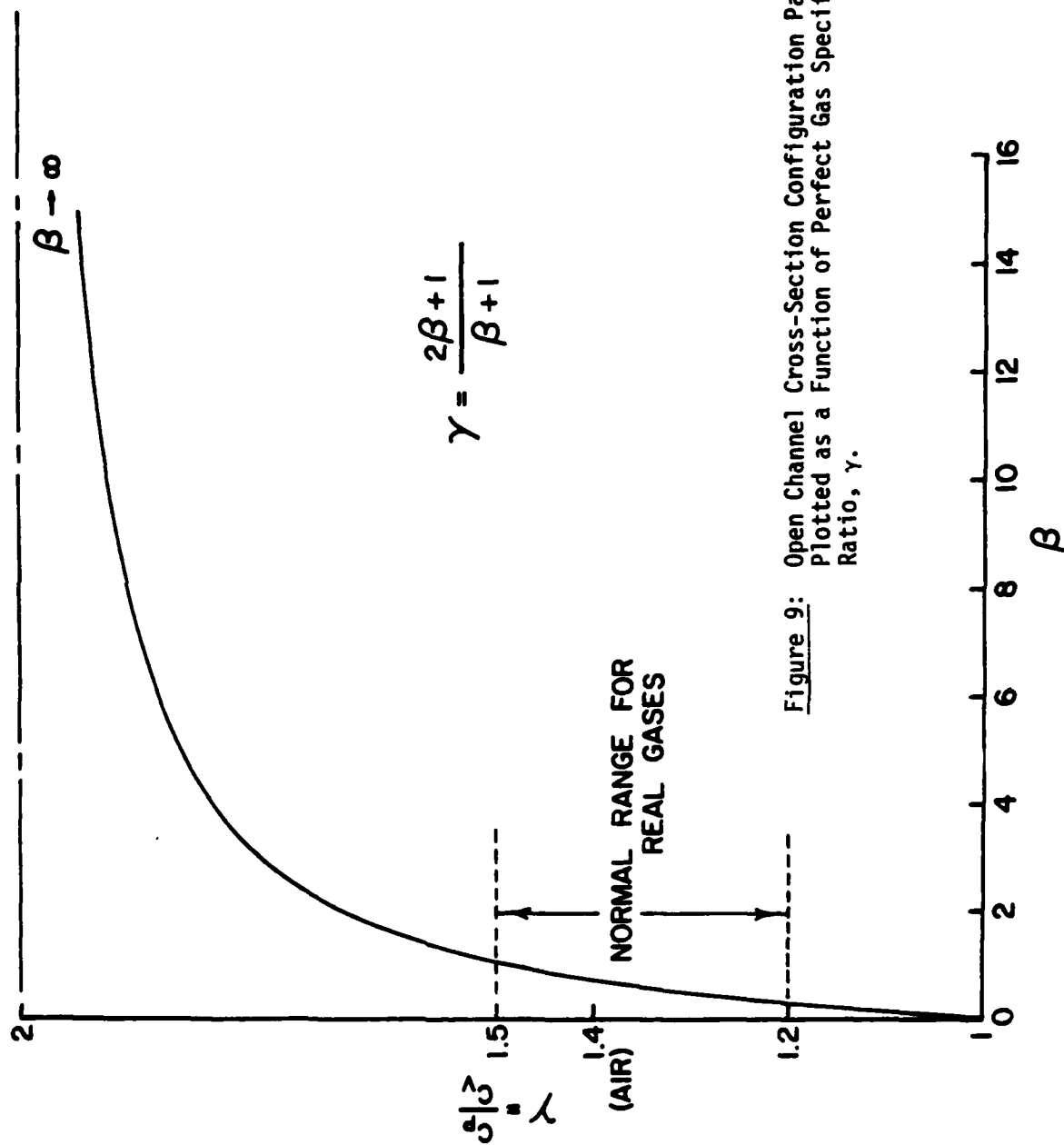
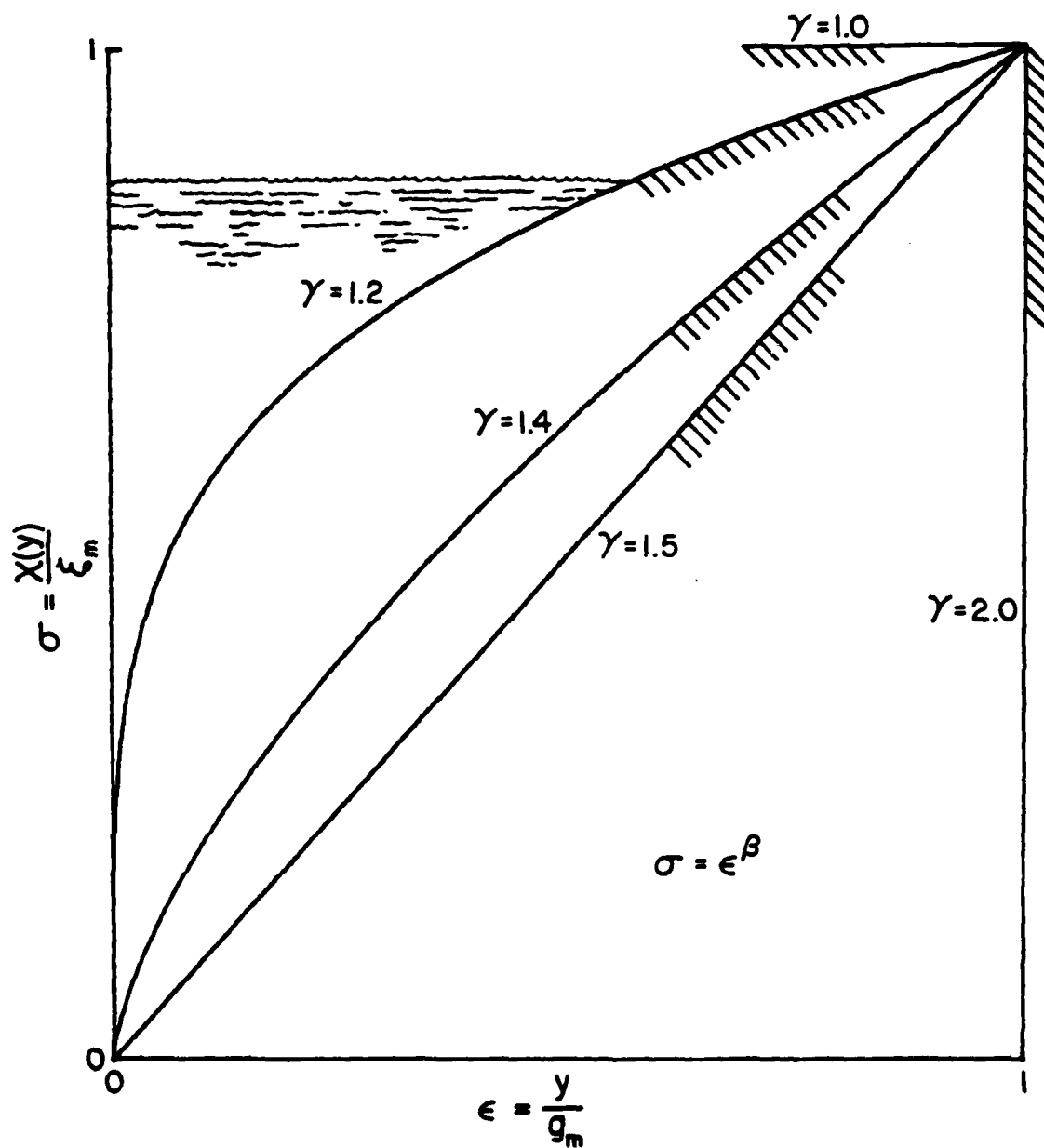


Figure 9: Open Channel Cross-Section Configuration Parameter, β , Plotted as a Function of Perfect Gas Specific Heat Ratio, γ .

Figure 10: Open Channel Cross-Sectional Geometries for the Perfect Gas Specific Heat Ratios 1.0, 1.2, 1.4, 1.5 and 2.0.



and the surface tension. For this reason, it was decided to pursue the experimental aspects of this investigation utilizing flow visualization and hydraulic analogue measurements in rectangular water channels as described in the section that follows.

SECTION VI

EXPERIMENTAL STUDIES OF WAKE DEVELOPMENT DOWNSTREAM OF A DOUBLE-CYLINDER CONFIGURATION

Experimental Arrangement

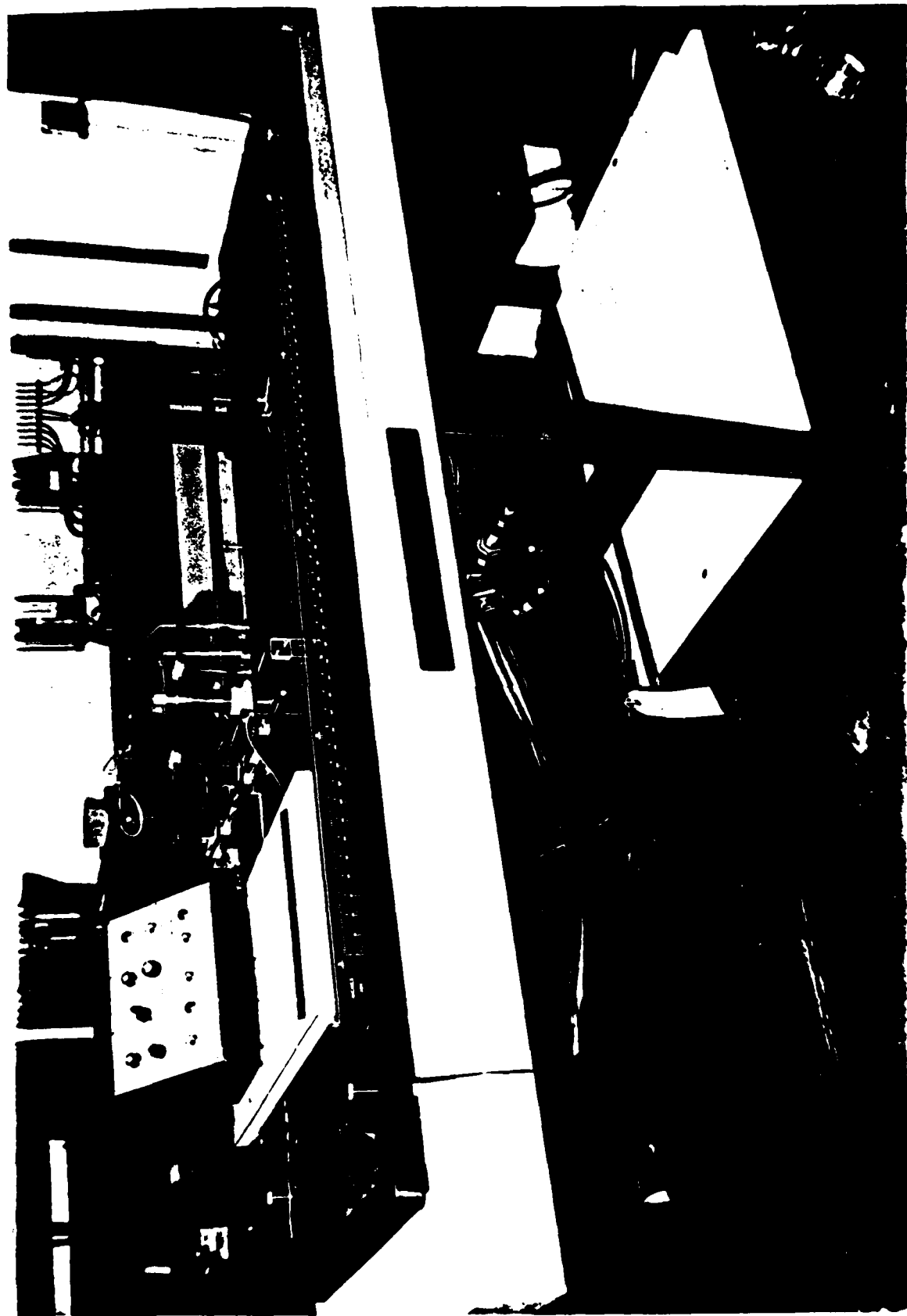
For this phase of the investigation, a TECHNOVATE Hydrodynamics System, Model 9093 was employed (Scott-Engineering Sciences, a division of A-T-O, Inc., 910 Southwest 12th Avenue, Pompano Beach, Florida 33060). This system, shown in Figure 11, consists of a shallow rectangular channel in which water is recirculated by a centrifugal pump, a precision level gage for wave height measurements, and a hydrogen bubble generator to allow for flow visualization. The channel working section measures 18 inches (45 3/4 cm.) wide by 2 1/2 inches (6 1/3 cm.) deep by 48 inches (122 cm.) long. Thus, the maximum depth-to-width ratio is 0.139 which reasonably satisfies the shallow, wide channel requirements of the hydraulic analogy. Moreover, the inlet tank and channel entrance are carefully profiled to provide satisfactory flow conditions, as are the working section length and discharge configurations. All are supplied in the form of an accurate reinforced glass fiber moulding which ensues a uniform smooth cross-section throughout.

The flow system is mounted by levelling screws on a robust fabricated steel frame fitted with casters for maneuverability. Beneath the frame, a centrifugal pump, controlled by a diaphragm type valve drives the channel fluid in a continuously recirculating pattern. The maximum pump output delivers 18 U.S. gallons per minute which is equivalent to a volumetric flow rate of .04 ft³/sec (7.48 U.S. gallons = 1 cubic foot) or 1135.7 cm³/sec. The minimum pump flow can be throttled all the way down to zero by controlling the diaphragm valve. Thus volumetric flow, ϕ , through the working section is given by:

$$0 \leq \phi \leq 1135.7 \text{ cm}^3/\text{sec}$$

which corresponds to an average fluid velocity of $\frac{\phi}{A_1}$, where A_1 is the fluid-filled cross-sectional area of the working section. Note that $A_1 = 2g_1\xi^*$, where $2g_1$ = the channel width = 45.75 cm, and ξ^* = the mean depth of the flowing liquid. Now recall that the Froude Number is defined by:

Figure 11: The Hydrodynamics Model 9093 Water Table used for Hydraulic Analogy Studies.



$$Fr = \sqrt{\frac{v^2}{\xi^* g_c}} = \sqrt{\frac{\phi^2}{4g_1^2 \xi^{*2} \xi^* g_c}}$$

Therefore, the relationship between Froude Number, volumetric flow and fluid depth for this hydrodynamics system is ($g_c = 981.5 \text{ cm/sec}^2$):

$$Fr = \sqrt{\frac{\phi^2}{\xi^{*3} (2.05 \times 10^6)}} \quad (53)$$

For $\phi = 0$, $Fr = 0$ and for $\phi = \phi_{\max} = 1135.7 \text{ cm}^3/\text{sec}$, $Fr = .793 \xi^{*-3/2}$. In

general, for a desired Froude number, the fluid depth may be varied depending upon the volumetric flow rate at which one chooses to operate the system. However, this is not entirely arbitrary, since the operating fluid depth must further take into account the growth of a boundary layer along the bottom of the channel -- a viscous effect which is neglected in the hydraulic analogy.

Hinze (1959 pg. 487) has suggested that the following equation may be used to obtain an estimate of the increase in boundary layer thickness, δ , with downstream distance, x , from the origin of a flat surface:

$$\frac{V \delta_m}{v} = 0.045 \left\{ \frac{Vx}{v} \right\}^{0.79} \quad (54)$$

where $\delta_m = 0.12\delta$ defines the momentum thickness and v is the kinematic viscosity of the fluid. Rearranging equation (54) and replacing δ_m by δ yields:

$$\delta = 0.375 \left\{ \frac{x}{v} \right\}^{0.21} \quad (55)$$

Assuming the fluid is water at room temperature ($68^\circ\text{F} = 20^\circ\text{C}$), its kinematic viscosity, v , is equal to 1.004 centistokes (Bolz and Tuve, 1970, pg. 67) which is $.01004 \text{ cm}^2/\text{sec}$. Furthermore, with

$$V = \frac{\phi}{2g_1 \xi^*} = \frac{\phi}{45.75 \xi^*}, \text{ equation (55) becomes:}$$

$$\delta = 0.318 \left\{ \frac{x}{\phi} \right\}^{0.21} \quad (56)$$

But, from the earlier definition of the Froude number, i.e., equation (53):

$$1432.33 (Fr) \xi^{*3/2} = \phi \quad (57)$$

From here, we see that, for a given depth, ξ^* , the Froude number increases directly with flow rate ϕ . Thus, at any operating depth, the maximum Froude number which can be achieved is limited by the maximum flow (1135.7 cm³/sec) that the recirculating pump can deliver. Substituting this value of ϕ into equation (57) yields equation (58) which is plotted in Figure 12:

$$(Fr)_{\max} = .793(\xi^*)^{-3/2} \quad (58)$$

Equation (58), or Figure 12 both indicate that to get up to a Froude number of at least unity in this flow system, the fluid depth must be reduced to about 8 millimeters at maximum pump output. If we incorporate this information into equation (56), i.e., let $\phi = 1135.7$ cm³/sec and $\xi^* = .857$ cm, we find that the growing boundary layer thickness, δ , has already reached fluid depth ξ^* when $x = 23.7$ cm, or, about 20% of the way into the channel. Beyond this point, the entire flow is in the boundary layer; and the situation worsens at lower Froude numbers because as ϕ is reduced for ξ^* held constant, the boundary layer thickens sooner with increasing x . The dimensions and flow characteristics of this particular water table thus seem to introduce a problem in terms of one of the assumptions inherent in the hydraulic analogy. To examine further the significance of this problem, let $\phi = 1135.7$ cm³/sec and combine equations (58) and (56) to get:

$$\delta = 0.318 \left\{ \frac{x}{x_L} \right\}^{.79} (121.92)^{.79} \frac{\xi^{*.21}}{\xi^*} \xi^* \left[\frac{1}{1135.7} \right]^{.21}$$

$$\text{Furthermore, writing: } (\xi^*)^{-.79} = [(\xi^*)^{-1.5}]^{.527}$$

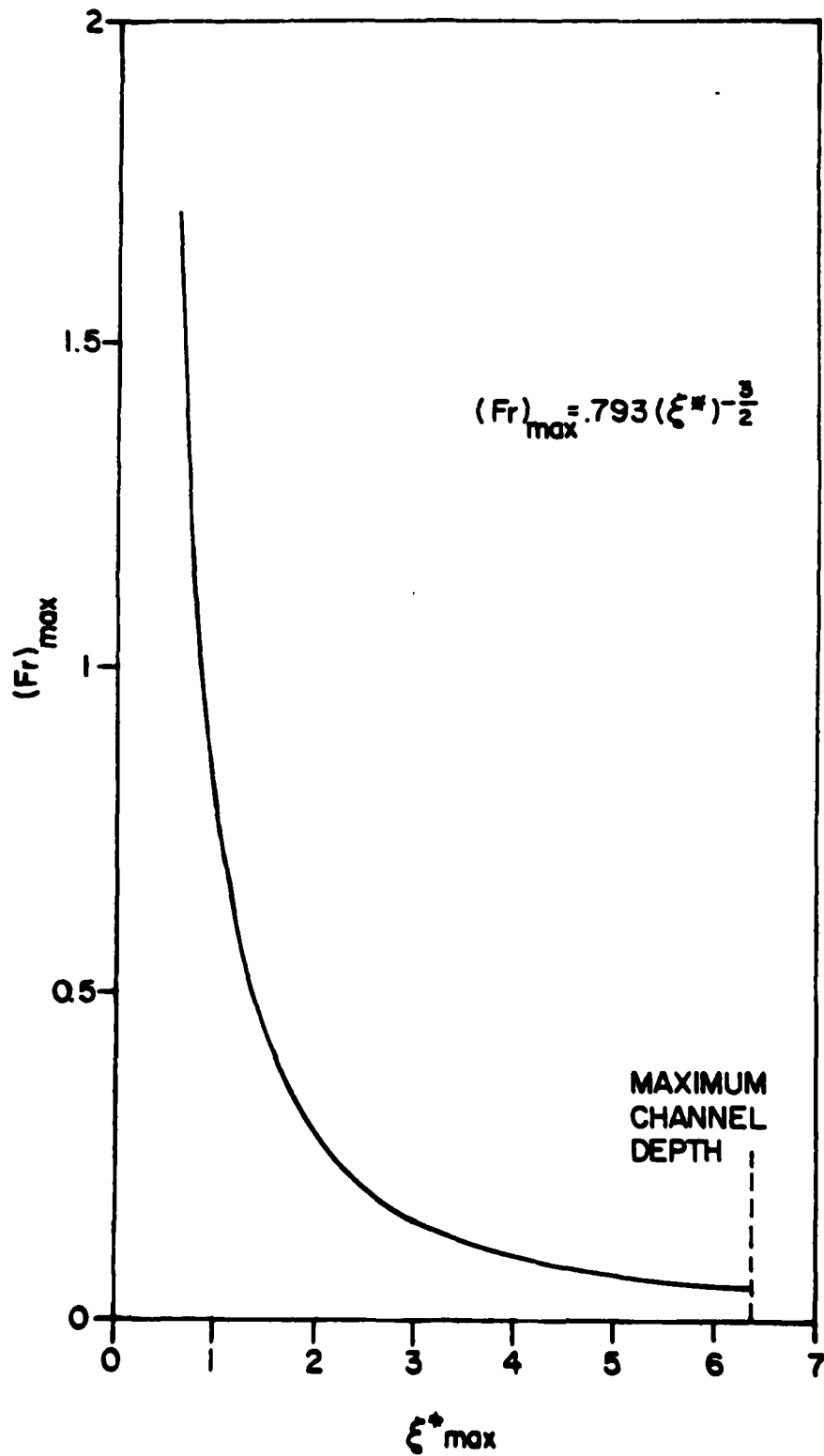
$$= \left(\frac{Fr_{\max}}{.793} \right)^{.527} \text{ from equation (58),}$$

$$\text{therefore: } \frac{\delta}{\xi^*} = 3.647 \left\{ \frac{x}{x_L} \right\}^{0.79} (Fr_{\max})^{.527} \quad (59)$$

where $x_L = 121.92$ represents the total length of the channel. Again, note that when $(Fr)_{\max} = 1$, $\delta/\xi^* = 1$ for $\frac{x}{x_L} = 0.194$ as already mentioned. On the other hand, if we set $\frac{\delta}{\xi^*} = 1$ for $\frac{x}{x_L} = 1$, then we find that $(Fr)_{\max} = .086$, which is much too low for our purposes. Any way that one views this situation, it clearly represents a source of error in the experimental arrangement. The extent of this error in terms of the hydraulic analogy will require further investigation, but its magnitude in the present flow system is highlighted by equation (59), which is also plotted in Figure 13 with $(Fr)_{\max}$ acting as a parameter. From these results, one would have to

conclude that all measurements made in the channel working section are being taken within the boundary layer of the flow. One possible way around

Figure 12: Maximum Froude Number vs. Water Depth for the Model 9093 Water Table.



BOUNDARY LAYER GROWTH

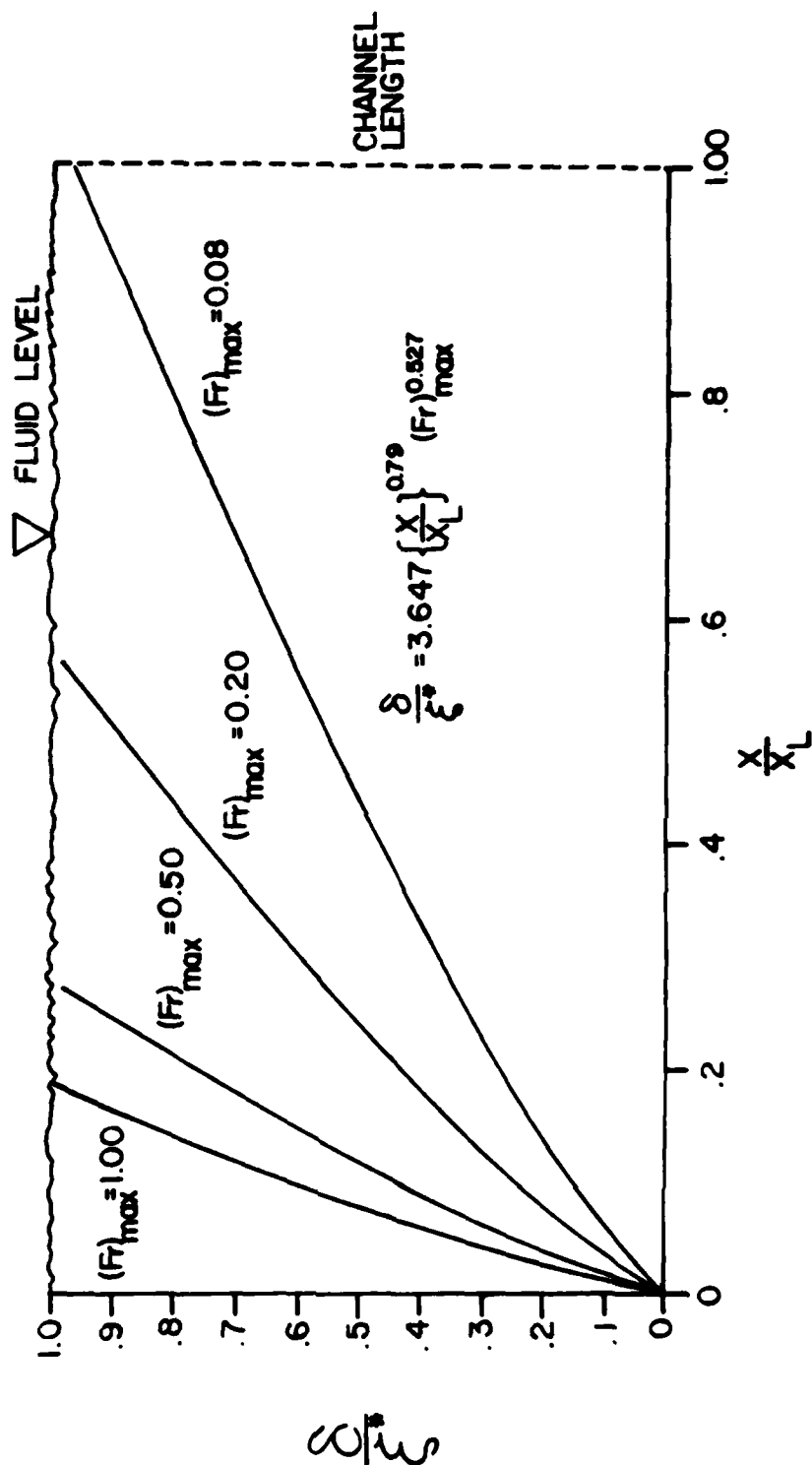


Figure 13: Boundary Layer Growth Along the Bottom of a Wide, Shallow, Open Rectangular Channel, as a function of Froude Number; (for Model 9093 Test Section).

this dilemma is to reduce the width of the channel using mountable plexi-glass plates supplied with model 9093. This would allow a deeper flow for the same cross-sectional area, but might adversely affect the depth-to-width ratio, which must be kept small. It is thus an option that must be considered carefully. Two other options are described below.

The growth of a boundary layer arises from frictional interactions between a moving fluid and a solid surface. One consequence of such interactions is a generalized tendency for the flow in the test section to be decelerated. This effect, however, may be cancelled approximately by introducing a gravity force obtained through tilting the channel by a small amount. The proper amount of tilt can be found most practically by trial and error. However, it, too, must be kept small because, in arriving at the analogue relationships, it was assumed that the water flow is two-dimensional. This assumption rules out significant vertical components of velocity and changes in water depth (the latter suggesting the use of large models compared with the water depth).

As a final point on boundary layer effects, it might be mentioned that viscous phenomena such as boundary layer growth may be accounted for, at least approximately, by matching as closely as possible the Reynolds Number of the Water Table Model Tests with that of the Aerodynamic Prototype experiments. Though this may often be difficult or impractical, one must still remember the point stressed earlier - that is, that a water channel can never give precise information on the behavior of a compressible fluid, but is best confined to a qualitative demonstration of the flow in or around a given model. Its major asset is that it can be used cheaply and conveniently to assess the relative merits of several versions of a design, prior to carrying out more exact investigations in a sub-or-supersonic wind tunnel.

Flow Visualization and Surface Wave Measurements

In the model 9093 Hydrodynamics System, the flow can be visualized either by the Hydrogen Bubble Technique (Schraub, Kline, et. al., 1965 and Davies and Fox, 1967) or by photographing surface wave patterns (Shapiro, 1949). The former utilizes as flow tracers small hydrogen bubbles evolved in water by electrolysis at a fine wire cathode which is positioned normal to the fluid flow (Figure 14). By careful illumination and photography, the paths traced out by these bubbles as they are carried along by the flow can be observed. Owing to their small size (.0005 to .0015 - inch diameter) they follow the flow accurately and their rate of rise due to the natural buoyancy of the light gas is small compared with the average rate of flow observed. Hence, the flow visualization obtained is sufficient for many purposes including those of this investigation.

The cathode consists of a fine stainless steel wire (.002-inch diameter) supported in tension by a two-pronged fork holder. The holder is grasped by a crocodile clip attached to the end of a rod which completes the electrical connection to the wire. The electrical lead hooked to the rod originates from the negative terminal of the pulse generator. This entire



Figure 14: Hydrogen-Bubble Generating
Unit on Hydrodynamics
Model 9093 Water Table

cathode arrangement can be positioned where required in the channel by a combination of clamps and rod holders attached to the tripod shown in Figure 14. The anode is located at the channel discharge end.

Since ordinary tap water can have a wide range of conductivities, the addition of a neutral salt is recommended in order to ensure the generation of a large number of small, equal-sized bubbles which are uniformly produced at various points along the wire. For this purpose, three liters of a saturated solution of sodium sulfate is added to the fluid in the channel, yielding an overall salt concentration of 25 grams per liter of channel fluid.

The hydrogen bubble generator produces "on" and "off" electrical pulses with provision for varying the off period, controlling the on period (pulse duration), and adjusting the D.C. Voltage. The adjustable time base permits quantitative velocity data analysis to be obtained by photographic means; while the variable D.C. Voltage is used to control bubble size, which is roughly proportional to current density. Normally, current densities of 1 to 2 amp/in² (6 to 12 ma per inch of wire) are sufficient to produce .001 to .0015-inch diameter bubbles from a .002-inch diameter cathode wire - and this is relatively independent of the velocity of flow past the wire.

To illuminate properly the hydrogen bubbles for photographic purposes, it is essential to provide a considerable amount of light in a fairly narrow flat beam, roughly parallel to the water surface (and below it) in a plane subtending between 90° and 110° to the line of sight of the observer. This is achieved in model 9093 by providing a self-contained light source (a cooled 55 watt tungsten iodine bulb backed by a concave mirror) and light guide (made of polished plexiglass) which enables the user to illuminate almost any part of the flow channel using the principle of total internal reflection. An example of what can be achieved is shown in Figure 15. Here, two stainless steel, 1" diameter cylinders have been immersed in the water channel to simulate the condition illustrated in Figure 1. The cylinders are rigidly fastened together as the flow is accelerated to show the double-vortex formation in the wake. Photographic records were obtained using a 400 ASA film with a wide aperture lens and an exposure of 1/30 th at f 2.8.

The flow visualization technique involving photography of surface wave patterns is based upon the fact that when diffuse light is reflected off of the flow surface, the troughs of the waves appear much brighter than the crests. Since the regions with higher waves correspond in the analogy to regions of high pressure, and vice versa, the light gradations on photographic records of the wave patterns can be calibrated to yield information about the pressure distribution in the flow field. Moreover, this technique also provides useful qualitative descriptions of the formation and behavior of streamline patterns and shock waves around different geometric configurations which intercept the flow.

Photography of wave patterns in the model 9093 can be accomplished conveniently by using high intensity spot lights; in this case, Berkey Colortran model 112-031 cine-queen 1000 watt lamps. A demonstration of the

Figure 15: Hydrogen Bubble Flow Visualization Downstream of Two, Tangent Stainless Steel, One-Inch Diameter Cylinders Immersed in the Water Channel with the Flow Travelling From Left to Right.



types of results that can be obtained with this lighting system is shown in Figure 16. Here, the spot lights have been reflected off the ceiling of the laboratory to produce a diffuse light and thus eliminate glare from the water surface. Moreover, the lights have been positioned so that the diffuse beam is reflected from the water surface directly into the camera lens when the water is absolutely still. This gives the observer a reference to the angle or slope of the water surface at any particular point. Recall that the subsequent troughs of the waves appear to be much brighter than the crests.

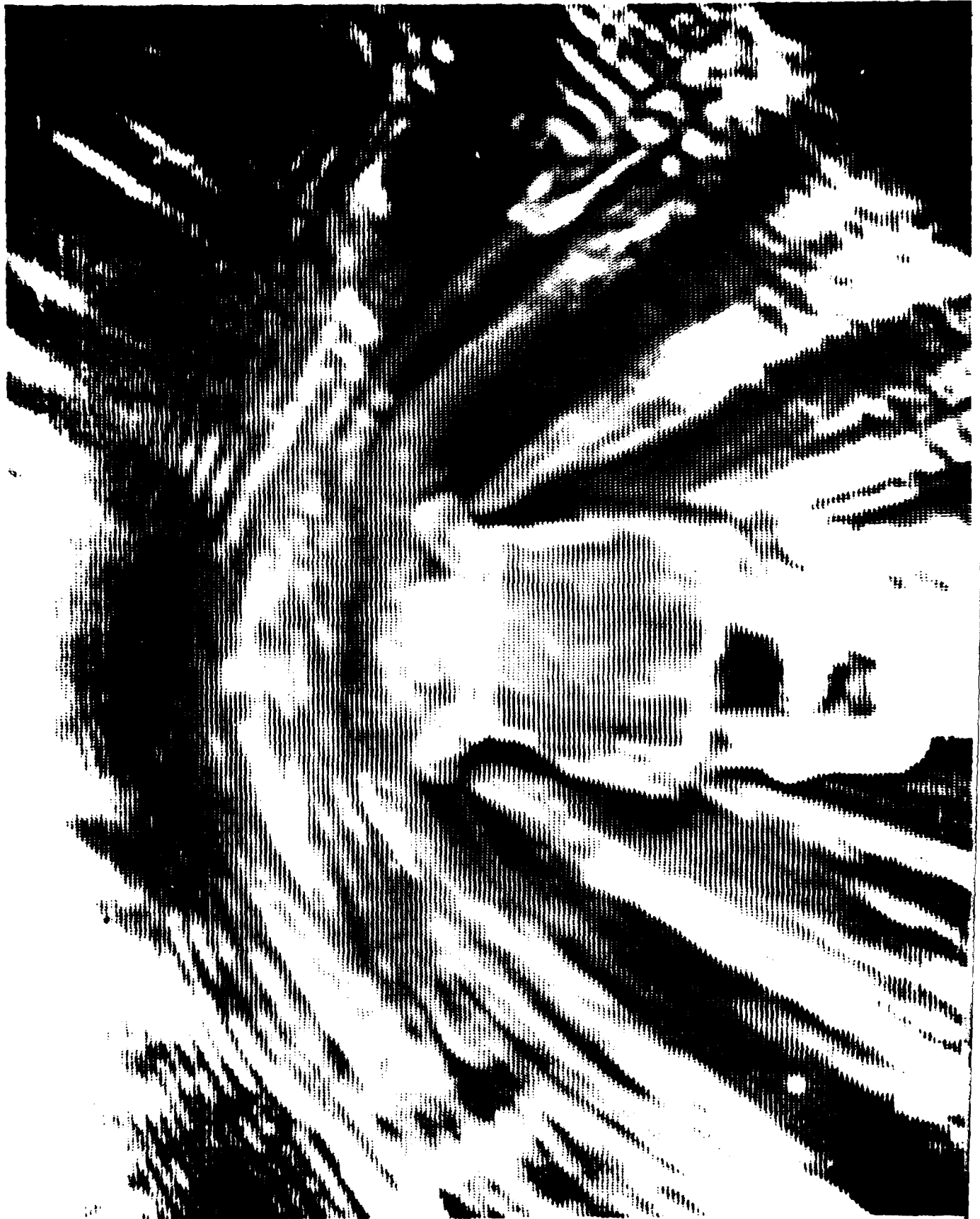
The flow photographed in Figure 16 is interacting with a simple plexiglass model of the arm and torso configuration. This model, shown in Figure 17, was scaled and constructed from anthropometric data such that the ratio of its frontal cross sectional area to that of the flow channel was 17:1. The arms were attached with wire loops passed through the eye-hooks, so that they could "swing" freely about the shoulders. The only restraint imposed was in the form of a plexiglass back rest that was built into the apparatus which held the model in place in the water table.

Figure 16 has been extracted for illustrative purposes from a 20-minute video-tape that was prepared to show the flow/model interactions for a range of Mach numbers. The Mach number in this particular photograph is 0.85, and several features should be noted. First, the large gap between wave patterns indicates a significant transition from a high pressure region in the front of the model to a low pressure region behind it. Second, one can see a developing bow shock wave, with a corresponding increase in pressure over the forward-facing parts of the model. Additional developing shocks (across which there is a fall in pressure) are in evidence along the wider parts of the model and at the trailing edges, where the pressure rises again. In particular, observe how the "arms" in this model have been thrown clear of the torso, and, although qualitative, how clearly one can visualize the developing flow patterns as an obstruction is placed in the oncoming flow. This is one of the key features of this technique as a means for understanding fluid behavior in a complex situation. Quantitative information concerning actual water level (hence, corresponding fluid pressure) can be further obtained by means of a built-in precision level gage which is an integral feature of model 9093. The gage has a calibrated depth probe which causes an indicator light on the control panel to come on as soon as the probe tip contacts the water surface. More details of the results observed on the 20-minute video tape are discussed below.

Results

In the experiments to be discussed the model shown in Figure 17 was held in place by a series of three laboratory clamps. These, in turn, were connected to the supportive structure which runs along the runners on the channel (see Figure 14). A five pound counter-weight was used to hold the model above the water such that it could be launched into a fully developed flow. The flow was controlled by the diaphragm valve described previously and the actual water speed was measured by timing a free-floating particle

Figure 16: Flow Visualization of Surface Wave Patterns Interacting with a Simple Plexiglass Model of the Arm-Torso Configuration. The Troughs of the Surface Waves Appear Much Brighter than the Crests.



ARM AND TORSO MODEL

MATERIAL: PLEXIGLASS
SCALE = 3 : 1

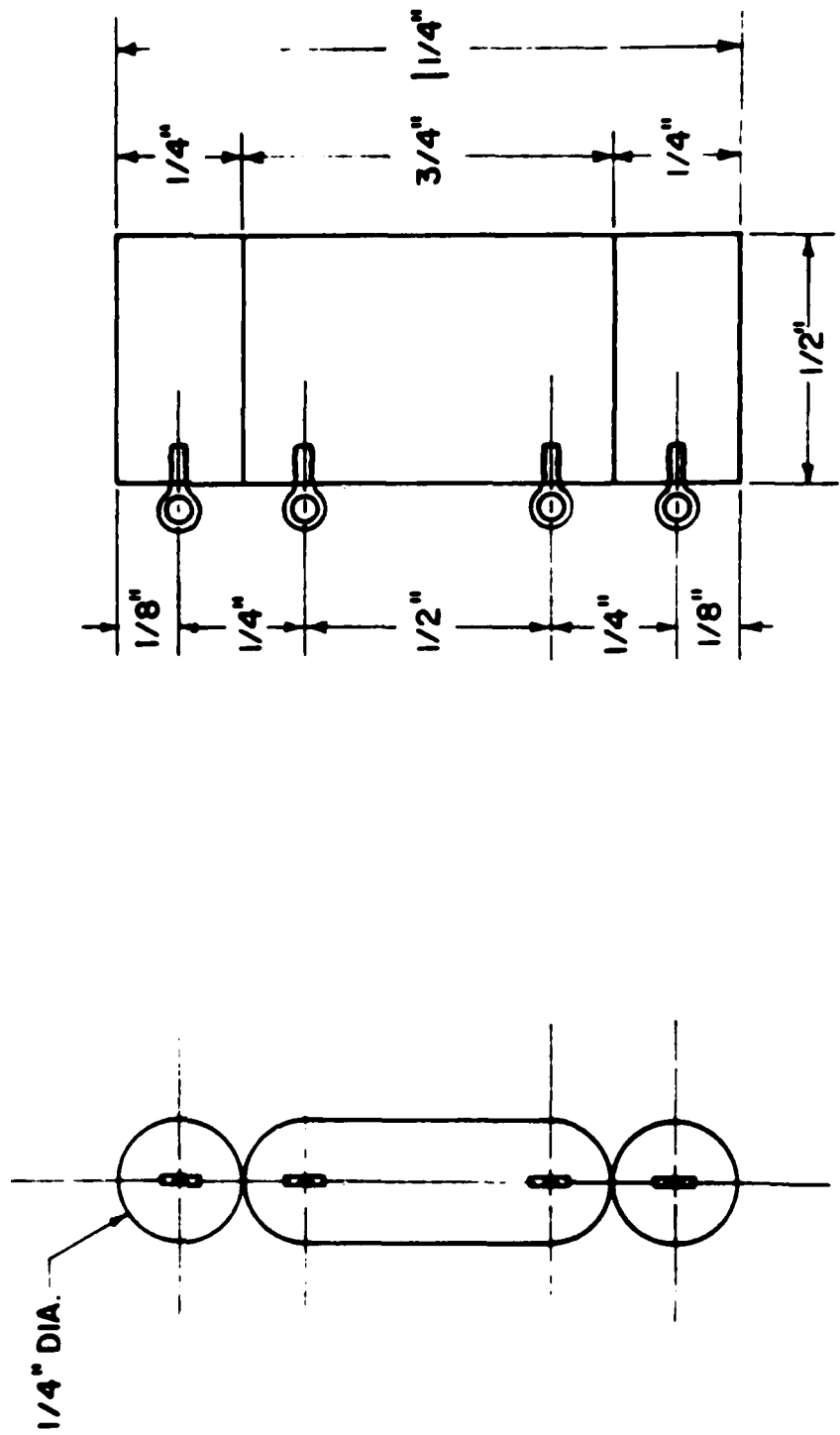


Figure 17: Simple Plexiglass Arm and Torso Model Used in Early Water Channel Flow Studies (see Figure 16).

as it traversed through a known channel distance. Two separate series of experiments were performed: in the first, the model was positioned in the water and the speed of the flow was increased gradually from zero to one which corresponds to an aerodynamic flow of Mach 1; in the second, the model was actually launched into pre-set and fully developed flows corresponding to the same set of Mach numbers, i.e., 0 to 1. Results of the first set of experiments are described in the next paragraph.

As the flow was gradually increased from zero, wave patterns formed first in front of the model, where stagnation points developed as fluid momentum was shifted 90° . The force build-up at such stagnation points had a tendency to pull the arms away from the torso, and this was clearly illustrated in the video tape. As the liquid flow rate continued to increase, the water level (ξ) continued to build up against the front of the model, indicating correspondingly higher pressures (see equation [51]) in the analogous aerodynamic system. Behind the model, in the wake region, the water level, and hence fluid pressures were much lower (see, for example, Figure 15 and 16). Eventually, the model became totally submerged and some vibration of the arms was noted. Vibration, or at least some slight oscillation in the arms was first observed at Mach 0.4. Recall that these are caused in part by the small opening created when the upper arms pull away from the torso, thus generating a Venturi-like effect which, coupled with gravity and the vortex street generated by this blunt-body configuration, drives the arms back towards the torso ... where stagnation forces cause the process to repeat itself. At Mach 0.6, the arms no longer touched the torso but still continued to vibrate slightly. The possibility of resonance effects coming into play due to phenomena such as these was suggested as possibly being influential in causing the ejection seat occupant to lose control of his or her arms, and flail injury may very well be the immediate result. At Mach 0.8, the limb displacement seemed to decline somewhat and the vibrations occurred at a lower frequency. This may have been due to the increasing frictional interaction between the arms and the back seat rest, and to less influence from gravitational effects because of the time scales involved. When the flow rate reached Mach 1, the model became completely submerged and virtually invisible to the above water observer. The water height ($\xi = 3$ to 4 times ξ_0) clearly indicated the presence of large forces tending to drive the arms away from the torso, and indeed, the arms flailed wildly even in this simple model of the actual ejection process. Moreover, the large increase in water level in front of the model was accompanied by a similar decrease in the water level behind the model, so that the total pressure drop across this geometric configuration was rather substantial for Mach Numbers in excess of 0.70. There was no arm-torso contact beyond Mach 0.5 and a continuous stream of fluid could be seen flowing in between the arms and the torso for this and higher Mach numbers.

Turning our attention now to results obtained utilizing the "launching" system described previously, it was observed that a simulated ejection taking place at Mach 0.4 has associated with it the development of some rather significant high pressure regions fore, and low pressure regions aft of the pilot-ejection-seat configuration. The pressure drop across the configuration was estimated to be some four times that of the free stream

dynamic pressure (i.e., $\xi = 2\xi_0$), which compares favorably with values predicted by the theory developed earlier. Furthermore, during this series of experiments, it was again observed that events start to get critical when ejection Mach numbers exceed 0.60. At this speed, the arms were thrown out violently when the model was launched suddenly into the flow and some slight oscillation of the limbs was noted. By the time the Mach number reached 0.8, a clearly defined oscillating wave pattern was set up behind the model due to the vortex street generated by flow separation effects. Also, the early stages of the formation of a bow shock wave could be seen as the fluid piled up in front of the model and successive crests of the bow waves became compressed, i.e., appeared closer together than before. Moving towards the rear of the model, one could see large gaps between wave patterns, indicating a rather significant transition from a high pressure region in front to a very low pressure region behind the model. Quantitative information concerning actual water level was obtained on the model 9093 by means of the built-in precision level gage and also by means of a specially designed small wave height measuring device (Bishop, G. H., 1980 and Cahill, B., 1981). Both methods revealed the presence of maximum pressure gradients on the order of 5 to 8 times that of the measured free-stream dynamic pressure, again agreeing rather well with theoretical predictions and verifying that the pilot ejected under similar circumstances would most likely suffer serious windblast and/or flail injury. At Mach 1, events were still further magnified, with large limb displacements, lower oscillation frequencies and violent shock/boundary-layer type interactions that were suggestive of serious potential consequences.

In summary, the experimental segment of this research program appeared to corroborate the theoretical formulation that predicted significant probability of flail for ejections occurring above Mach 0.70. Based on these confirming observations, some concluding points are presented in the next section.

SECTION VII

CONCLUDING REMARKS

This research program has examined the serious problem of windblast from both the theoretical and experimental points of view. The mathematical theory developed, although greatly simplified for purposes of tractability, nevertheless revealed the essential physics which leads to limb flailing. That is, the theory clearly identified fluid dynamic stagnation and flow separation forces as first-order effects which contribute to the dislodgment and subsequent flailing of the limbs of an ejection seat occupant. These effects are strongly dependent upon the angle at which the pilot intercepts the air stream, and they become significant and quite serious for ejections taking place above Mach 0.7. To confirm these findings, a series of water table experiments was performed in which flow stagnation and separation effects were, indeed, seen to be primary causes of windblast and flail phenomena. Both qualitative and quantitative

measurements of the flow patterns revealed that the critical Mach number at which the aerodynamics of windblast becomes potentially harmful is around 0.6, and beyond that point flail is almost assured. Parameters of significance for design purposes include the trajectory of the ejection process, the geometry of the ejection configuration and the speed of ejection. All of these are not suited for supersonic ejections as presently designed and significant changes appear to be necessary in order to insure the safety of the aircrew during combat missions.

SECTION VIII

PUBLICATIONS, PROJECTS AND THESES THAT RESULTED FROM THIS RESEARCH AND WERE SUPPORTED ENTIRELY OR IN PART BY FUNDS FROM THIS AFOSR GRANT

1. Technical Report: "Studies of Limb-Dislodging Forces Acting on an Ejection Seat Occupant," Schneck, Daniel J.; USAF(AFSC)-AMD, Aerospace Medical Research Laboratory Technical Report Number AMRL-TR-78-103, January, 1979. Available from the National Technical Information Service, NTIS # AD-A064-882/4GA.
2. Expanded Abstract and Paper Presented: "Aerodynamic Forces Exerted on an Articulated Body Subjected to Windblast," Schneck, D.J.; in: Maio, D., (Editor), Annual Review of Air Force Sponsored Basic Research in Environmental and Acceleration Physiology, Proceedings of a Conference held at the U. S. Air Force Academy, September 12-13, 1978, Page 21.
3. Expanded Abstract and Paper Presented; "Studies of Limb-Dislodging Forces Acting on an Ejection Seat Occupant," Schneck, D. J.; in: Proceedings of the Annual Scientific Meeting of the Aerospace Medical Association, Sheraton Park Hotel, Washington, D.C., May 14-17, 1979, Pages 250-251.
4. Senior Project: "Hydrodynamic Flow Visualization of High Speed Pilot Ejection," Bishop, G; Senior Project and Report completed May 29, 1979 under the direction of faculty advisor Dr. Daniel J. Schneck.
5. Technical Report: "Aerodynamic Forces Exerted on an Articulated Human Body Subjected to Windblast -- Part II.," Schneck, D. J.; Virginia Polytechnic Institute and State University, College of Engineering, Technical Report Number VPI-E-79-30, September 1979, Pages i-iii and 1-24.
6. Expanded Abstract and Paper Presented: "Aerodynamic Forces Exerted on an Articulated Body Subjected to Windblast," Schneck, D.J.; in: Irving, G. W.. III, (Editor), Annual Review of Air Force Sponsored Basic Research in Environmental and Acceleration Physiology, Proceedings of a Conference held at St. Louis University Medical Center, October 2-4, 1979, Page 6.

7. Technical Report: "On The Causes and Consequences of Windblast Forces Associated with High-Speed Ejections," Schneck, D. J.; Virginia Polytechnic Institute and State University, College of Engineering, Technical Report Number VPI-E-80-6, September, 1980, Pages i-vii and 1-51.
8. Paper: "Studies of Limb-Dislodging Forces Acting on an Ejection Seat Occupant," Schneck, Daniel J.; Aviation, Space and Environmental Medicine, Volume 51, Number 3, Pages 256-264, March, 1980.
9. Expanded Abstract and Paper Presented: "On The Aerodynamics of Windblast," Schneck, D. J.; in: Irving, G. W., III (Editor), Annual Review of Air Force Sponsored Basic Research in Environmental Physiology and Biomechanics, Proceedings of a Conference held at the University of Kentucky, September 23-25, 1980, Paper Number 26, Page 41.
10. Senior Project: "Small Wave Height Measuring Device," Cahill, Bret; Senior Project and Report completed May 25, 1981 under the direction of faculty advisor Dr. Daniel J. Schneck.
11. Masters' Thesis and Technical Report: "Applications of a Z-80 Microcomputer System to Laboratory Data Acquisition," Greco, S.; Masters' Thesis completed August, 1981 under the direction of faculty advisor Dr. Daniel J. Schneck. Virginia Polytechnic Institute and State University, College of Engineering, Technical Report Number VPI-E-81-21, Pages i-vii and 1-92.
12. Manuscript in Preparation: "On The Aerodynamics of Windblast," Schneck, Daniel J.; to be submitted to Aviation, Space and Environmental Medicine.
13. Technical Report: "On The Aerodynamics of Windblast," Schneck, Daniel J.; Virginia Polytechnic Institute and State University, College of Engineering, Technical Report Number VPI-E-81-31, November, 1981.

REFERENCES

- Bolz, R. E., and Tube, G. L., (Editors), Handbook of Tables for Applied Engineering Science, Cleveland, Ohio, The Chemical Rubber Co., 1970.
- Davis, W., and Fox, R. W., "An Evaluation of the Hydrogen Bubble Technique for the Quantitative Determination of Fluid Velocities Within Clear Tubes," Journal of Basic Engineering, Vol. D89, Pgs. 771-781, December, 1967.
- Gradshteyn, I. S., and Ryzhik, I. M., Table of Integrals, Series, and Products, New York, Academic Press, Inc., 1965.
- Harleman, D. R. F., and Crossley, H. E., Jr., "Studies on the Validity of the Hydraulic Analogy to Supersonic Flow -- Part IV," Wright Air Development Center, Aircraft Laboratory Report No. AF-TR-5985, February, 1952.
- Hinze, J. C., Turbulence, New York, McGraw-Hill Book Company, Inc., 1959.
- Horner, T. W., and Hawker, F. W., "A Statistical Study of Grip Retention Force," Aerospace Medical Research Laboratory, Technical Report No. AMRL-TR-72-110 (AD 767904), May 1973.
- Ippen, A. T., and Harleman, D. R. F., "Studies on the Validity of the Hydraulic Analogy to Supersonic Flow -- Parts I and II (May), Part III (October)," Wright Air Development Center, Aircraft Laboratory Report No. AF-TR-5985, 1950.
- Landweber, L., "Flow About a Pair of Adjacent, Parallel Cylinders Normal to a Stream," Navy Department, The David W. Taylor Model Basin, Technical Report No. 485, Washington, D.C., July, 1942.
- Milne-Thomson, L. M., Theoretical Hydrodynamics, New York, The MacMillan Company, Third Edition, 1955.
- Preiswerk, E., "Application of the Methods of Gas Dynamics to Water Flows with Free Surface -- Part I. Flows with no Energy Dissipation," N.A.C.A. Technical Memorandum Number 934, March 1940.
- Preiswerk, E., "Application of the Methods of Gas Dynamics to Water Flows with Free Surface -- Part II. Flows with Momentum Discontinuities (Hydraulic Jumps)," N.A.C.A. Technical Memorandum Number 935, March, 1940.
- Schneck, D. J., "Aerodynamic Forces Exerted on an Articulated Body Subjected to Windblast," Aerospace Medical Research Laboratory Report No. AMRL-TR-76-109 (AD-A044 217/8GA), December, 1976.
- Schneck, D. J., "Studies of Limb-Dislodging Forces Acting on an Ejection Seat Occupant," Aerospace Medical Research Laboratory Report No. AMRL-TR-78-103 (AD-A-64 882/4GA), January, 1979.

Schraub, F. A., Kline, S. J., Henry, J., Runstadler, P. W., Jr., and Littell, A., "Use of Hydrogen Bubbles for Quantitative Determination of Time-Dependent Velocity Fields in Low-Speed Water Flows," Journal of Basic Engineering, Vol. D87, Pgs. 429-444, June, 1965.

Shapiro, A. H., "An Appraisal of the Hydraulic Analogue to Gas Dynamics," Massachusetts Institute of Technology Meteor Report No. 34, 1949.

Streeter, V. L., (Editor), Handbook of Fluid Dynamics, New York, McGraw-Hill Book Company, Inc., 1961.

Whicker, L. F., "The Development of the Hydraulic Analogy," M.S. Thesis in Applied Mechanics, Virginia Polytechnic Institute, Blacksburg, Virginia, May, 1951.

**DAT
FILM**